République Algérienne Démocratique et Populaire

Ministère de l'Enseignement Supérieur et de la Recherche Scientifique

**UNIVERSITÉ CHADLI BENDJEDID - EL TARF** الشاذلي بن جديد-الطارف

FACULTÉ DES SCIENCES ET DE LA TECHNOLOGIE
DÉPARTEMENT DE PHYSIQUE

# MÉMOIRE DE MASTER

**DOMAINE : SCIENCE DE LA MATIÈRE**

**FILIÈRE :** Physique

**OPTION :** Physique des Matériaux

## Thème

# Synthesis by coprecipitation and determination of magnetic, structural and morphological properties of ferrite nanoparticles

**Présentée par :**
**MIRA Amina**

**Dirigée par :**
**DEBBOUB Salima**

**Jury de soutenance :**

| | | | |
|---|---|---|---|
| REDJATI Yosra | Président | MCB | Université -El Tarf |
| DEBBOUB Salima | Rapporteur | MCB | Université -El Tarf |
| ZOUAGHI Zoubir | Examinateur | MAB | Université -El Tarf |

**Année Universitaire : 2024/20225**

# *Dedication*

***my dear parents,***

*To the two people whose love and sacrifices have shaped the person I am today,*

*Thank you for being my strength, for your endless support, and for always believing in me.*

*This work is dedicated to you with all my love and gratitude.*

***my sisters,***

*For your kindness, encouragement, and presence in every step of the way—thank you.*

***celia,***

*to my best friend, who is more than just a friend , she is a sister to me—thank you for always standing by my side.I dedicate this work to you, with all my love.*

# Acknowledgments

*Praise be to God, whose blessings and guidance have been the foundation of my success, Without His grace, none of this would have been possible.*

I would like to express my sincere gratitude to the members of the research team, Mr. T. Tahraoui and my supervisor Mrs. Salima Debboub, had suggested this topic, and whose contribution was pier to make the successful completion of this study. Their dedication, expertise, and commitment were influential to reach our research objectives. Thank you for the constructive criticism and the useful suggestions.
I would like again to express my deep appreciation to my supervisor for her valuable guidance, patience, and constant support throughout the completion of this work, her encouragement and confidence were a great source of motivation for me.

I thank Mrs. Yosra Redjati and Mr. Zoubir Zouaghi for being members of the Jury to evaluate this work.

I would like to extend my heartfelt appreciation to Mrs. Safia Alleg, Director of the LM2S Laboratory, Badji Mokhtar-Annaba University, and Mr. A. Manseri for their invaluable contributions to characterize the sample with the laboratory equipments.

I am also indebted to Sofiane Kherici for his assistance and crucial remarks for the synthesis of the sample.

I also extend my gratitude to all the teachers of the Faculty of Sciences and Technology, for the knowledge, dedication, and mentorship they have provided during my academic journey.

My heartfelt thanks go to my beloved family, for their endless love, prayers, and belief in my abilities.

# Abstract

Our study is mainly based on the study of the structural, morphological and magnetic properties of manganese-cobalt spinel ferrite nanoparticles $Mn_{0,5}Co_{0,5}Fe_2O_4$. These nanoparticles were synthesized by the coprecipitation method and characterized with three techniques. X-ray scattering (XRD) analysis has confirmed the cubic spinel crystal structure of ferrites, in fact it leads to identify the crystalline phases from the diffractogram peaks and to determine its lattice parameters. On the other hand, the average crystallite size of about 40 nm is computed by Scherrer formula. Scanning electron microscopy (SEM) indicates quasi-spherical nanoparticles, the grains have an average size in the order of 60 nm. This value is slightly higher than that found by XRD. Both qualitative and quantitative analysis by means of energy dispersive spectroscopy (EDS) is also carried out to check the chemical composition of the sample and the spatial distribution of the chemical elements which are iron, manganese, cobalt and oxygen. Spinel ferrite nanoparticles possess magnetic properties which are ascertained with using a vibrating sample magnetometer (VSM), the results obtained showed a soft ferromagnetic material. In fact, these nanoferrites have potential applications in several fields.

# Résumé

Notre étude repose essentiellement sur l'étude des propriétés structurales, morphologiques et magnétiques des nanoparticules de ferrites spinelles de manganèse-cobalt $Mn_{0,5}Co_{0,5}Fe_2O_4$. Ces nanoparticules ont été synthétisées par la méthode de coprécipitation et caractérisées par trois techniques. L'analyse par diffraction des rayons X (DRX) a confirmé la structure cristalline spinelle cubique des ferrites, elle nous a permis d'identifier les phases cristallines à partir des pics du diffractogramme et de déterminer ses paramètres de maille. D'autre part, la taille moyenne des cristallites d'environ 40 nm a été calculée par la formule de Scherrer. La microscopie électronique à balayage (MEB) a montré des nanoparticules quasi-sphériques, les grains ont une taille de l'ordre de 60 nm. Cette valeur est légèrement supérieure à celle trouvée par DRX. Une analyse qualitative et quantitative par spectroscopie à dispersion d'énergie (EDS) a été également réalisée pour vérifier la composition chimique de l'échantillon et la répartition spatiale des éléments chimiques qui sont le fer, le manganèse, le cobalt et l'oxygène.

Les nanoparticules de ferrites spinelles possèdent des propriétés magnétiques qui ont été déterminées à l'aide d'un magnétomètre à échantillon vibrant (VSM), les résultats obtenus ont montré un matériau ferromagnétique doux. En réalité, ces nanoferrites ont de potentielles applications dans diverse domaines.

# ملخص

يعتمد هذا العمل بشكل أساسي على دراسة الخصائص البنيوية، المورفولوجية والمغناطيسية لجسيمات نانوية من نوع فيريت سبينيل المنغنيز والكوبالت $Mn_{0,5}Co_{0,5}Fe_2O_4$ التي تم الحصول عليها باستعمال طريقة الترسيب المشترك وقد تم توصيف العينة بواسطة ثلاث تقنيات مختلفة. أكدت التحاليل الخاصة بتقنية حيود الأشعة السينية (XRD) البنية البلورية المكعبة وهي البنية التي تتميز بها فيريتات السبينيل، و كذلك عن طريق هذه التقنية تمكنا من تحديد الأطوار البلورية الخاصة بالعينة وذلك من خلال استغلال قمم مخطط الحيود و تمكنا أيضا من تحديد ثوابت الشبكة البلورية . ومن ناحية أخرى، تم حساب حجم البلورات باستعمال علاقة شيرر و قدر بحوالي 40 نانومتر. أظهرت الصور المتحصل عليها عن طريق المجهر الإلكتروني الماسح (SEM) جسيمات نانوية شبه كروية، حيث يبلغ حجم الحبيبات حوالي 60 نانومتر و لوحظ أن هذه القيمة تفوق بقليل تلك التي تم الحصول عليها عن طريق XRD. زيادة على ذلك تم إجراء تحليل نوعي وكمي بواسطة مطيافية الطاقة المشتتة (EDS) للتحقق من التركيب الكيميائي للعينة و كيفية توزيع العناصر الكيميائية بداخلها وتتمثل هذه العناصر في الحديد، المنغنيز، الكوبالت والأكسجين.

تمتلك أيضا جسيمات فيريت السبينيل النانوية خصائص مغناطيسية تم تحديدها باستخدام مقياس مغناطيسية العينة المهتزة (VSM) وأظهرت النتائج أن هذه العينة عبارة عن مادة حديدية ممغنطة عالية الأنفاذية و لينة . في الواقع لجسيمات فيريتات السبينيل النانوية تطبيقات هامة في عدة مجالات.

# Table of contents

**Chapter III**
**Results and discussions**

# List of symbols

| | |
|---|---|
| A | Tetrahedral cationic site |
| B | Octahedral cationic site |
| $n_1$ | Number |
| $n_2$ | Number |
| $\nu_1$ | Valence of the ion |
| $\nu_2$ | Valence of the ion |
| $\lambda$ | Degree of inversion |
| a | Lattice parameter |
| R | Ionic radius |
| M | Molar mass |
| d | Density |
| $N_A$ | Avogadro number |
| M | Magnetization |
| $\vec{a}$ | Vector |
| $\vec{b}$ | Vector |
| $\vec{c}$ | Vector |
| $\vec{t}$ | Vector that defined the translations group |
| h, k, l | Miller indices |
| $d_{hkl}$ | Reticular distance |
| (h k l) | Reticular plane |
| $\Delta$ | Path difference of radiations |
| $\lambda$ | Wavelength of the radiation |
| $\theta$ | Bragg angle |
| n | Interference order |
| $S_{(hkl)}$ | Area |
| P | Reflective power |
| $I_0$ | Intensity of the incident radiation |
| $\Delta_k$ | Full width at half maximum |
| $\beta_k$ | Integral width |
| $y_{max}$ | Height |
| $D_{cris}$ | Average crystallite size |
| K | Scherrer constant |
| e | Potential difference |
| $d\Phi$ | Flux variation |
| $M_S$ | Saturation magnetization |
| $H_C$ | Coercive field |
| $M_r$ | Remanent magnetization |
| $M_t$ | Maximum transverse magnetization |
| G | Magnetic field |

# List of abbreviations

| | |
|---|---|
| XRD: | X-ray diffraction |
| SEM: | Scanning electron microscopy |
| EDS: | Energy dispersive X-ray spectrometry |
| WDS: | Wavelength dispersive spectroscopy |
| VSM: | Vibrating sample magnetometer |
| NPs: | Nanoparticles |

# List of figures

# List of tables

# Introduction

In this work, the samples preparation is carried out at the laboratory of the National Higher School of Technology and Engineering (ENSTI) of Annaba and their characterization has been done at the Laboratory of Magnetism and Spectroscopy of Solids (LM2S), Physics Department, Badji Mokhtar-Annaba University.

Since nanotechnology covers a wide technological fields whose common factor is the nanometric size of structures, and the main goal is largely based on the development of nanomaterials in various shapes [1].

Among the most studied nanomaterials in recent years, one can mention nanometric spinel ferrites of type $MFe_2O_4$ (M = Ni, Zn, Co,…etc.). Investigations of their physicochemical properties integrate several fields of chemistry, mechanics, physics, information storage, biomedical, etc. They show an advantage of existing in the form of nanoparticles (NPs) either aggregates or nanoparticles coated in a given matrix and also in the form of nanostructured powders. These different configurations are widely used in various fields. These materials with semiconducting properties have already been the subject of numerous works both at the fundamental and applied level, but they continue to generate a lot of interest in the fields of catalysis and photocatalysis [2,3,4].

This experimental work is particularly focused in nanomaterials based on spinel ferrites in powder shape whose particles have nanometric sizes. This material belongs to the complex oxides family of transition metals with spinel structure.

In this work, the selected process for the magnetic nanoparticles synthesis of manganese-cobalt spinel ferrites $Mn_{0,5}Co_{0,5}Fe_2O_4$ is coprecipitation, which is a chemical modus operandi. This is the most used and reported synthesis route in the literature. This choice depends on the advantages it presents such as simplicity, cost, synthesis time and in particular yield. In addition, it allows the generation of nanometric-sized crystallites for magnetic, catalytic and electronic applications.

The manuscript is includes into three parts:

The first chapter is devoted to a literature review on the different ferrite structures and properties of spinel ferrites. An overview of nanoparticles is also provided.

The second chapter presents entirely the experimental techniques for the synthesis and characterization of nanoparticles developed to study their structural, microstructural and magnetic properties. First, we will describe the principle of the coprecipitation method and its own advantages and disadvantages. Second, we will describe the techniques of X-ray diffraction (XRD), scanning electron microscopy (SEM) and vibrating sample magnetometry (VSM).

The third chapter includes all the prevailed results. The first part of this chapter describes the synthesis protocol of manganese-cobalt spinel ferrite nanoparticles. The second part concerns the characterization of NPs with distinct techniques.

Finally, a general conclusion displays the main results and grants possible perspectives related to the study of other properties to broaden the scope of application for these spinel oxide nanoparticles.

# Chapter I

# Background information on nanoparticles and spinel ferrites

In this chapter, a bibliographic search is mainly afforded to nanomaterials, nanoparticles, spinel ferrites and their physicochemical and magnetic properties.

## I.1. Nanomaterials classification

A nanomaterial is a material with at least one external dimension on the nanoscale, then with an internal or surface structure on the nanoscale (between 1 and 100nm).

In fact, nanotechnology has become a major scientific and economic issue in lifestyle. The unique properties of nanomaterials are virtually expanding their applications in every sector. Intensive research is being conducted on the use of nanomaterials in energy storage and conversion, pharmaceuticals, photovoltaic cells, catalysis, composite materials, food, cosmetics, medicines and diagnostics, construction products, biomedicine, electronics, food processing, telecommunications, agriculture.

Their presence raises many questions about the risks they may pose, both to human health and the environment. Nanomaterials can be classified into five categories:

### I.1.1. Origin classification

According to their origin, nanomaterials are divided into two classes: natural nanomaterials and synthetic nanomaterials.

### I.1.2. Structural configuration and composition classification

According to their structural composition, nanomaterials can be classified into four groups: organic/dendrometers, inorganic, carbon-based and composites.

### I.1.3. Dimensional classification

Nanomaterials are ranked into four types based on their dimensions: 0D, 1D, 2D and 3D.

### I.1.4. Pore dimensions classification

Nanomaterials are arranged into three groups according to pore size: microporous materials, mesoporous materials, and macroporous materials.

### I.1.5. Toxicity classification

Nanomaterials are classified into three groups according to their potential toxicity: fibrous nanoparticles, persistent granular nanoparticles and CMAR (carcinogenic, mutagenic, asthmatic and toxic for reproduction) nanoparticles [5,6].

## I.2. Classification of NPs

The International Organization for Standardization (ISO) describes NPs as nano-objects whose external dimensions are all in the nanoscale, where the lengths of the longest and shortest axes do not significantly differ.

NPs come in various sizes, shapes, and structures. They can be spherical, cylindrical, conical, tubular, hollow-core, spiral, etc., or irregular. Their sizes range from 1 to 100 nm. If the size is less than 1 nm, they are generally referred to as atomic aggregates. NPs can be crystalline, monocrystalline, polycrystalline, or amorphous. They can be free-standing or in the form of agglomerations. NPs can be uniform or composed of multiple layers. NPs are generally classified according to their composition into three classes:

### I.2.1. Organic NPs

This class includes NPs made of proteins, carbohydrates, lipids, polymers, or any other organic compound. The most prominent examples of this class are dendrimers, liposomes, micelles, and protein complexes such as ferritin. These NPs are generally non-toxic, biodegradable, and sometimes such as liposomes, may have a hollow core. Organic NPs are sensitive to thermal and electromagnetic radiation. Various parameters dictate the potential application of organic NPs, such as composition, surface morphology, stability, and load capacity.

### I.2.2. Carbon-based NPs

This class includes NPs that consist solely of carbon atoms. Examples include fullerenes, carbon black NPs, and carbon quantum dots. Due to their unique electrical conductivity, high resistance, electron affinity, optical, thermal, and sorption properties, carbon-based NPs have a wide uses such as drug delivery, energy storage, bioimaging, photovoltaic devices, microbial ecology, or microbial pathogen detection. Carbon nanodiamonds and carbon nanoonions are more complex carbon-based nanoparticles.

### I.2.3. Inorganic NPs

This class includes metallic, ceramic, and semiconductor nanoparticles. Some metallic nanoparticles have interesting thermal, magnetic, and biological characteristics. These materials are used to develop nanodevices. Nowadays, the synthesis of metallic nanoparticles with controlled size, shape, and facets is essential for the creation of advanced materials.

Semiconductor nanoparticles are composed of semiconductor elements. These NPs have unique wide band gaps, forming important materials for photocatalysis, optics, and electronic devices.

Ceramic nanoparticles are inorganic solids consisting of carbonates, carbides, phosphates, and oxides of metals and metalloids. They are generally produced with heat and successive cooling and come in amorphous, polycrystalline, dense, porous, or hollow forms. They are mainly used in biomedical applications due to their high stability and load-carrying capacity. However, they are also used in other applications such as catalysis, dye degradation, photonics, and optoelectronics [7,8].

## I.3. General information on spinel ferrites

### I.3.1. Layout of spinel

Structure of spinel is a widespread mineral that set up at high temperatures in the cubic crystal system. It is found in basic igneous rocks (gabbros, basalts, peridotites, etc.), in silica-poor metamorphic rocks, and sometimes in granulite-facies rocks. It is an amazing stone with a vast collection of spinels of very good quality, in several shapes and sizes and various colors. The main deposits are in Sri Lanka and Myanmar. Afghanistan, Australia, Brazil, Nigeria, Madagascar and Tanzania also produce it; spinel is often found in the same deposits as corundums [9].

Spinel is a mineral species belonging to the oxide family. Its various colors are attributed to traces of chromium, iron, and vanadium. Its chemical formula is $MgAl_2O_4$ (magnesium aluminum oxide).

For a long time, red spinel has been confused to other stones such as ruby or sapphire, but it was recognized as a gem in its own right in 1581. Spinel gems, octahedral in shape, have a strength of 8 on the Mohs scale. Its luster is vitreous and has an attractive transparency and few inclusions in the heart of the stone.

Spinel comes in a variety of colors, each more stunning than the last. It has a straightforward refraction that has allowed it to be distinguished from ruby.

The spinel structure was first observed in 1915 by William Henry Bragg and Yoshio Nishikawa [10]. A detailed description of this structure was subsequently given by other authors, the spinel lattice has a cubic structure.

**Fig.I.1**: Spinel gemstone

**Fig.I.2**: Spinel crystals [9]

Spinels have the general chemical formula $AB_2O_4$, in which A and B represent the cations and O the anions. In spinel-structured oxides, the anions are larger ions (r = 0,14 nm), forming a face-centered cubic lattice, defining tetrahedral A and octahedral B cationic sites [9].

The spinel unit cell can be divided into eight a/2 stop cubes. In two cubes sharing a face or a vertex, the ionic positions are different, but they are identical in two cubes sharing only one edge. It is sufficient to represent the ionic positions in two adjacent cubes to describe the total structure. This arrangement leads to the formation of 64 tetrahedral sites that are occupied by A cations and 32 octahedral sites that are occupied by B cations. Each of these eight partial cubes contains 4 oxygen atoms that describe a tetrahedron [9].

One A ion and three B ions, together with the oxygen ion, constitute a unit that can be considered the basic unit of the spinel lattice. Each A and B ion is respectively surrounded by four and six oxygen ions. The O-A direction is that of one of the diagonals of the cube, and the O-B direction coexists with its edges. The induced lattice parameters of spinels are generally between 8 and 8,11Å [9].

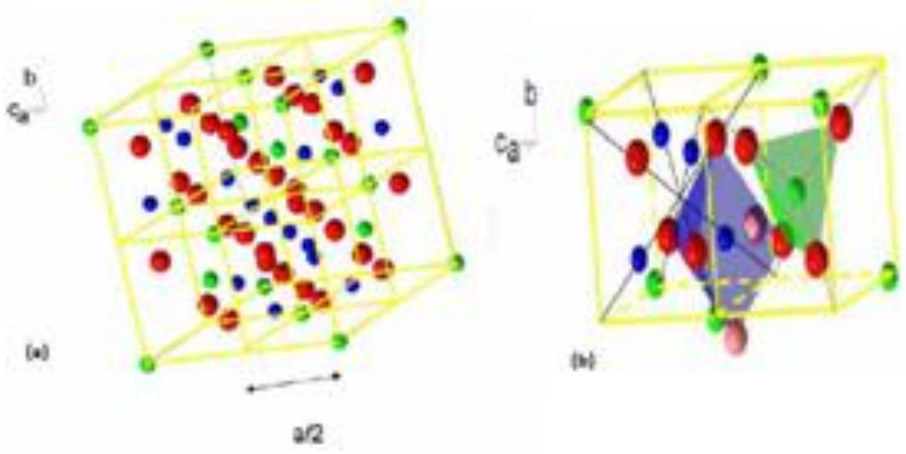


**Fig.I.3:** (a) Primitive edge mesh divided into eight cubes
(b) Zoom on two adjacent cubes [9]

The different factors that contribute to the total energy of the lattice in spinels are:

- elastic energy
- electrostatic energy (Madelung)
- polarization effects

Above all, both of two energies are sufficient to determine the total ionic energy of metal oxides. The elastic energy refers to the degree of distortion in the crystal structure due to the difference in ionic radii, assuming that the ions adopt a spherical shape. Cations with ionic radii between 0,225 and 0,4Å should occupy the tetrahedral sites, while cations with radii between 0,4 and 0,73Å should occupy the octahedral sites [9].

### I.3.2. Polycrystalline ferrites

There are three families of ferrites that are distinguished by three different structural symmetries; garnet, hexagonal and cubic. The physicochemical properties of spinel ferrite depend on the types of cations in the lattice, also on their distributions in the available sites in the crystal. The state of a cation (valence and environment) is affected on a large number of factors that are specific to it but also dependent on the other surrounding metallic species [11,12,9].

#### I.3.2.1. Garnet structure ferrites

The general formula of these ferrites is $M_3Fe_5O_{12}$ where M is usually a rare earth ion. They have a cubic crystallographic structure and their name comes from the fact that they have similar structure as the garnet $Mn_3Al_2Si_3O_{12}$. They are soft materials (low coercive field). They are used in the microwave range and are considered as the basis of non-reciprocal devices. An example is yttrium iron garnet $Y_3Fe_5O_{12}$ (YIG) [13].

#### I.3.2.2. Hexagonal ferrites or hexaferrites

$MFe_{12}O_{19}$ ferrites have a hexagonal crystallographic structure. They are magnetically hard materials (high coercive field) since they have a strong uniaxial anisotropy. They are mainly used to manufacture permanent magnets. Examples include barium hexaferrites ($BaFe_{12}O_{19}$) and strontium hexaferrites ($SrFe_{12}O_{19}$) [13].

#### I.3.2.3. Spinel structure ferrites

Spinel ferrites or cubic ferrites are magnetic oxides, they have the general formula $MOFe_2O_3$ or $MFe_2O_4$ which is also expressed in the form $M^{+2}Fe_2^{+3}O_4$ such that $M^{+2}$ is a bivalent metallic cation and $Fe_2^{+3}$ is the trivalent iron cation, they have selfsame crystallographic structure as the mineral spinel $MgAl_2O_4$. The unit cell of spinel ferrite belongs to the cubic structure and the cube is made up of 8 molecules of $MOFe_2O_3$ [14,13].

### I.3.3. Physicochemical properties of spinel ferrites

Ferrites are mixed oxides with spinel structure, space group Fd3m (see number 227 in international tables) and chemical formula $MFe_2O_4$ where M is a divalent metal ion ($Co^{+2}$, $F^{+2}$, $Zn^{+2}$, $Mn^{+2}$, $Ni^{+2}$, $Mg^{+2}$, $Cu^{+2}$, etc.). The oxygen ions form a face-centered cubic (FCC) lattice, defining tetrahedral and octahedral cationic sites. The tetrahedral sites will be appointed by the notation A and the octahedral sites by the notation B.

The elementary mesh of the spinel lattice comprises 32 $O^{-2}$ anions and 24 metal cations is distributed within the 64 tetrahedral sites of which only 8 sites are occupied by metal ions and limited by

four oxygen ions, and 32 octahedral sites of which 16 sites are occupied and limited by six oxygen ions (Fig I.4). According to the distribution of divalent and trivalent ions in the tetrahedral (A) and octahedral (B) sites, 2 types of spinels are defined, direct and inverse spinels [15,12].

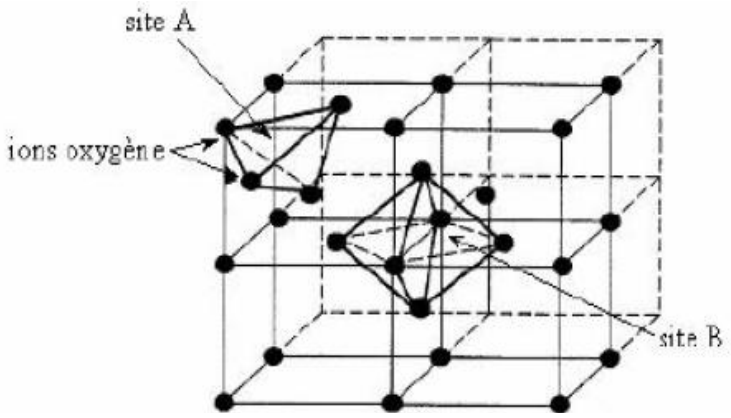


**Fig.I.4**: Crystal structure of spinel ferrite [15]

The total positive valence of the ions, relative to four oxygen atoms, must naturally be equal to 8. On the assumption that the preceding rules are respected and that the diameters of the ions are not too different, all combinations, all replacements are possible. These compounds will have the formula $M_{n_1}^{\nu_1} Fe_{n_2}^{\nu_2} O_4$.

Where $n_1 + n_2 = 3$. The numbers $n_1$ and $n_2$ must verify the relation $n_1\nu_1 + n_2\nu_2 = 8$ where $\nu_1$ and $\nu_2$ are the valences of the two ions.

The distribution of ions on the two sites A and B depends on several parameters: the diameter of the ions, their electronic structure and the electrostatic energy. The two distances that separate an ion to the oxygen atoms that surround it are relatively different for the two sites (0,25 a for site A and 0,216 a for site B, a being the lattice parameter), so that the larger ions tend to occupy the octahedral sites, and the smaller ones occupy the tetrahedral sites [13].

### I.3.3.1. Cation distributions in spinel ferrites

Spinels carry divalent and trivalent ions are classified relative to $MgAl_2O_4$ spinel according to whether the divalent cation occupies the A sites or the B sites. The existence of tetrahedral and octahedral sites within the face-centered cubic lattice of $O^{-2}$ ions allows variable ionic distributions among these two crystallographic sites. These cationic arrangements can be described by the degree of inversion λ. The distribution of cations in the different sites is written as follows:

$$A_{1-2\lambda}^{+2}\ B_{2\lambda}^{+3}\ \left[A_{2\lambda}^{+2}\ B_{2-2\lambda}^{+3}\right] O_4^{-2} \qquad (1.1)$$

Where λ is the inversion rate or degree of inversion ($0 \leq \lambda \leq 0.5$)

As the temperature increases, the migration of cations between the different crystallographic sites is favored and the degree of inversion increases. The complexity of the spinel structure comes primarily from the large number of cations that can be enclosed by it.

**I.3.3.1.1. Normal spinel** ($\lambda = 0$)

In fact, in the mixed oxide $MFe_2O_4$, where the radius of the divalent ion is smaller than that of the trivalent ion (R(Fe) > R(M)), $Fe^{+3}$ ions can occupy the B sites, while the smaller $M^{+2}$ ions settle the A sites. This is called normal structure.

Normal or direct spinel is distinguished by divalent cations that occupy the tetrahedral A sites and trivalent $Fe^{+3}$ cations on the octahedral B sites. The distribution of cations in the different sites is expressed as follows:

$$[M^{+2}]_A\ [Fe_2^{+3}]_B O_4^{-2} \qquad (1.2)$$

Zinc ferrites $ZnFe_2O_4$ and cadmium ferrites $CdFe_2O_4$ have an ionic distribution of this nature [12,13].

**I.3.3.1.2. Inverse spinel** ($\lambda = 0.5$)

In the mixed oxide $MFe_2O_4$ where the radius of the divalent ion is larger than that of the trivalent Fe ion (R(Fe) < R(M)), the $M^{+2}$ ions tend to settle the octahedral sites, where they have more space, thus forcing some of the $M^{+2}$ ions to occupy the tetrahedral sites. When the replacement is complete, all the A sites are occupied only by $Fe^{+3}$ ions. The B sites are setttled by both $M^{+2}$ and $Fe^{+3}$ ions. This is called an inverse structure.

Therefore, when divalent cations occupy B sites, the spinel is said to be inverse. It has been shown that the ion distribution can be done in another way, that is, the $M^{+2}$ cations occupy half of the octahedral sites while half of the trivalent $Fe^{+3}$ cations are placed in tetrahedral A sites and the other half in octahedral B sites. In other words, the cations are distributed over both octahedral and tetrahedral sites in equal proportions. The distribution of cations in the different sites is written as follows:

$$[Fe^{+3}]_A\ [M^{+2}Fe^{+3}]_B O_4^{-2} \qquad (1.3)$$

The most well-known inverse spinels are cobalt ferrites $CoFe_2O_4$, nickel ferrites $NiFe_2O_4$ and copper ferrites $CuFe_2O_4$ [12,13].

**I.3.3.1.3. Complex (mixed) spinel** ($0 < \lambda < 0.5$)

Thus, the ionic radius is introduced in order to set forth the inversion in spinels. This is the ideal case of the compound $MgAl_2O_4$. The $Mg^{+2}$ ions, too large to be in position A, are placed in position B, thus rejecting a part of the $Fe^{+3}$ ions, smaller, in the A sites. This rule is not general, there is also the affinity of certain ions for the A or B sites. For example, the $Zn^{+2}$ ions have an ionic radius identical to that of $Co^{+2}$, yet zinc ferrite has a normal structure while cobalt ferrite has an inverse structure. The rule

can be applied to the ions with perfect spherical symmetry $Li^{+}$, $Mg^{+2}$, $Al^{+3}$, $Ti^{+4}$ as well as to the ions whose d layer is half filled, $Mn^{+2}$, $Fe^{+3}$. The affinity for tetrahedral sites can originate from the $4_{s,p}$ or $5_{s,p}$ electrons involved by the metal ions in the covalent bonds with oxygen such as the case for the $Zn^{+2}$ or $Cd^{+2}$ ions [13].

Spinel is said to be statically disordered. The divalent cations $M^{+2}$ and the trivalent cations $Fe^{+3}$ are distributed on both the tetrahedral A site and the octahedral B site. The formula of the compound is expressed as:

$$\left[M_{1-\lambda}^{+2}Fe_{\lambda}^{+3}\right]_{A}\left[M_{\lambda}^{+2}Fe_{2-\lambda}^{+3}\right]_{B}O_{4}^{-2} \qquad (1.4)$$

Manganese ferrites $MnFe_2O_4$ are characterized by an ionic distribution of this nature [15,12].

These intermediate structures are directly linked to the inversion parameter. This parameter depends essentially on the heat treatment conditions and more particularly on the partial pressure of oxygen and the cooling rate.

In general, there is a real competition between the different ions to settle the octahedral and tetrahedral sites. It is then possible to state the magnetic moment of each of the two sublattices only by introducing the average moment. The theoretical density is deduced from the molar mass M(g/mol) and the lattice parameter a by the formula: $d = 8M / a^3N_A$ $(g/cm^3)$, where $N_A$ is the Avogadro number [13].

### I.3.4. Magnetic properties of spinel ferrites

The magnetic properties of ferrites are directly related to the chemical composition and the arrangement of atoms in the tetrahedral and octahedral sites. Indeed, the interaction is stronger when the atoms make an angle of 180˚, this is the case for atoms of two different sites type A−B, this is the theory of superexchange. The relay of the superexchange couple is the anion $O^{-2}$. The coupling intensity depends on the nature of the two cations, but also on the length and angle of the M–O–M bonds. The coupling is intense when the latter is closest to 180˚. On the other hand; as the bonds are longer as the coupling is weaker.

The three possible types of superexchange coupling are into cations of A sites and B sites (A–B coupling), betwixt cations of A sites (A–A coupling) and between cations of B sites (B–B coupling). The resulting magnetic order depends on whether the couplings are ferromagnetic or antiferromagnetic. The B–B coupling is antiferromagnetic but the A–B coupling, also antiferromagnetic, is stronger so B–B is frustrated. If the magnetic moment in the A site decreases, the A–B coupling becomes weaker and the B–B coupling is no longer frustrated [13].

All magnetic materials can be classified into four categories (diamagnetic, paramagnetic, ferromagnetic, ferrimagnetic, and antiferromagnetic) based on their response to an external magnetic field applied at room temperature.

A typical property of a ferromagnet is that the magnetization M shows a hysteresis cycle depending on the applied magnetic field. Moreover, this magnetization is a very complicated function of the applied magnetic field, the temperature and also the previous processing that the sample has undergone, i.e. the successive previous magnetic fields that have acted on the material.

According to the property of magnetizing or demagnetizing, on the value of coercivity and on the shape of hysteresis cycles, magnetic materials can be ranked into three groups; soft magnetic materials, hard magnetic materials and support materials for magnetic recording [16].

## I.4. Application of spinel ferrites

Due to their amazing magnetic properties and higher corrosion resistance, spinel ferrites are useful in numerous applications including [17]:

- ***Sensors***: ferrite nanoparticle-based sensors possess exceptional sensitivity, low detection limits, and high signal-to-noise ratios. The detection of variations in humidity is one of the most common uses of sensors. Typically, humidity sensing is primarily attributed to the surface effects of the interaction between water vapor and solids. Ceramic-based humidity sensors that utilize metal oxides have shown superior performance in terms of physical stability, thermal capability, mechanical strength, and chemical resistance [2].
- ***Photoluminescent applications***: mixed spinel nanostructures such as $CoFe_2O_4$, $NiFe_2O_4$, and $ZnFe_2O_4$ are known for their photoluminescence at room temperature, which is considered one of their most significant properties. The spectrum of photoluminescence offers insights into various characteristics such as surface oxygen vacancies, defects, charge carrier trapping, and transfer efficiency [2].
- ***Magnetic applications***: materials possessing high coercivity are referred to as hard materials, whereas those with low coercivity are termed soft materials. Inductor cores, transformers, and microwave devices are made of soft materials, while permanent magnets are made of hard materials. In general, soft ferrites are characterized by a low coercivity value, and their magnetization can be adjusted, making them suitable for advanced electronic engineering purposes, such as transformer cores, high-frequency inductors, and microwave component [2].
- ***Dielectric applications***: for example, $NiFe_2O_4$ has a dielectric structure consisting of conducting grains and grain boundaries. The transfer of electrons between $Fe^{2+}$ and $Fe^{3+}$ ions and holes between $Ni^{3+}$ and $Ni^{2+}$ ions enables electrical conduction and dielectric polarization. However, at higher frequencies, the electron/hole exchange frequency cannot keep up with the applied electric field, leading to lower polarization [2].

- ***Waste water treatment***: the roles of spinel ferrite nanoparticles include their potential use as an adsorbent for pollutants and their ability to catalyze the degradation of organic pollutants under photocatalytic conditions [2,18].
- ***Catalytic applications***: spinel ferrites are commonly used as heterogeneous catalysts due to their ease of recovery from reaction mixtures by filtering or using an external magnetic field, making the process cost-effective and environmentally friendly through their multiple recyclings. To be economically valuable and ecologically friendly, heterogeneous catalytic nanoparticles play a key role in the selective protection of functional groups [2].
- ***Photocatalytic applications***: ferrites have a wide surface area and many reaction sites due to their small crystallite size, which increases photocatalytic activity. The effectiveness of photocatalysis depends on various factors such as the choice of photocatalyst, size of the nanoparticles, level of crystallinity, accessibility of the active surface to pollutants, and resistance to diffusion of organic pollutants. These parameters can significantly impact the photocatalytic properties of the material. Small particle size and high crystallinity are important factors that enhance the specific surface area and active sites, leading to improved photocatalytic activity. Ferrites are excellent candidates for photocatalysis due to their spinel crystal structure and bandgap that can absorb visible light. They are capable of degrading a wide range of contaminants [2].
- ***Coloring***: for example, $CoFe_2O_4$ is a black pigment that is frequently used in the ceramic industry. The performance of the pigment is affected by the coating crystallization, with a higher number of crystals in the glass leading to a brighter color. $ZnFe_2O_4$ NPs have a high covering power and a low cost and are thermally stable, insoluble, and resistant to aggressive media. $ZnFe_2O_4$ spinel pigments react with the corrosive environment, producing cationic soaps that enhance the binder's mechanical strength and reduce solubility. During the process of annealing, the color of $ZnFe_2O_4$ may be affected by both the particle size and the annealing temperature. This is because annealing can result in a reduction in the total reflecting surface of the powder, which can have an impact on the overall color [2].
- ***Biomedical applications***: for use in biomedical applications, magnetic nanoparticles need to have high magnetic saturation values and be biocompatible, while also being stable and non-agglomerated when dispersed in water. These nanoparticles can be used within individual cells to facilitate magnetic fluid hyperthermia, drug delivery, and stimulation of metabolic pathways through thermal excitation. $MnFe_2O_4$ nanoparticles have attracted significant interest in the field of biomedicine due to their desirable properties, including simple synthesis, controllable size, high magnetization value, superparamagnetic nature, ability to be monitored by an external magnetic field, and high biocompatibility. The surface modification of $MnFe_2O_4$ NPs by incorporating them into mesoporous $SiO_2$ nanospheres or coating them with mesoporous $SiO_2$ can enhance the stability of the

nanoparticles in water, improve their biocompatibility, and prevent their agglomeration and degradation.

$CoFe_2O_4$ NPs has been utilized for medication administration, imaging, and brain tumor therapy in general.

Magnetic hyperthermia is a recently developed supplementary treatment for malignant tumors that involves the use of appropriate magnetic nanoparticles in a magnetic field, generating heat that aids in the elimination of damaged tissues at a temperature ranging between 41 and 46°C [2,19].

# Chapter II

## Experiment and characterization

In the first part of this section, one describes the synthesis process for the acquired spinel ferrite nanoparticles. Subsequently, we will define in brief the different precursors used in the synthesis with coprecipitation. The last part of this chapter focuses on the experimental techniques used to reach the structural, microstructural, morphological and magnetic properties of these nanoparticles. The features of spinel ferrites are highly dependent on the selected method for synthesis, so the preparation method can be chosen according to the required application.

## II.1. Synthesis of spinel ferrites by coprecipitation

Spinel ferrites are synthesized using various methods, including solvothermal, hydrothermal, sol-gel, microemulsion, thermal decomposition, auto-combustion, and coprecipitation. Then, each of these methods has obviously its own advantages and hindrances [10,20].

### II.1.1. The coprecipitation Principle

This is one of the earliest methods for the synthesis of spinel ferrites. It allows the production of precipitates from metal chloride precursors dissolved in distilled water; these solutions interact with sodium hydroxide (NaOH) added to them to form nanometric powder. In other words, a basic solution is added to solutions of metal salts containing divalent and trivalent cations. In fact, metal chloride hexahydrate and tetrahydrate salts have been utilized as precursors.

For the synthesis of manganese-cobalt spinel ferrite powder, it is reached with mixing the homogeneous solution of $Fe^{+3}$ (iron III chloride hexahydrate + distilled water), the homogeneous solution of $Co^{+2}$ (cobalt II chloride hexahydrate + distilled water), the homogeneous solution of $Mn^{+2}$ (manganese II chloride tetrahydrate + distilled water) and by adding sodium hydroxide. The mixture of metal ion solutions is stirred up and heated higher speed.

Furthermore, to produce spinel-structured ferrite materials, the synthesis procedure requires precise adjustment of pH, which is generally achieved using ammonium or sodium hydroxide solutions.

After rinsing and filtering, the brownish precipitate must be dried at 100°C and then annealed at a temperature of approximately 600°C for 6 hours. Manganese-cobalt ferrite nanoparticles are obtained after cooling [10,21].

### II.1.2. The co-precipitation advantages and drawbacks

This method is easy to implement and have other merits such as:

- better homogeneity of the salt mixture obtained during precipitation.
- higher product purity.
- morphology control is possible.

- a large specific surface area.
- no use of organic solvents.
- lower cost.
- synthesis or reaction time is on the order of a few minutes.
- higher yield.
- heat processing not require high temperatures [22,12].

However, co-precipitation has drawbacks, including:

- difficulty in controlling stoichiometry.
- aggregates can form during synthesis.
- use of a concentrated basic medium [15,12].

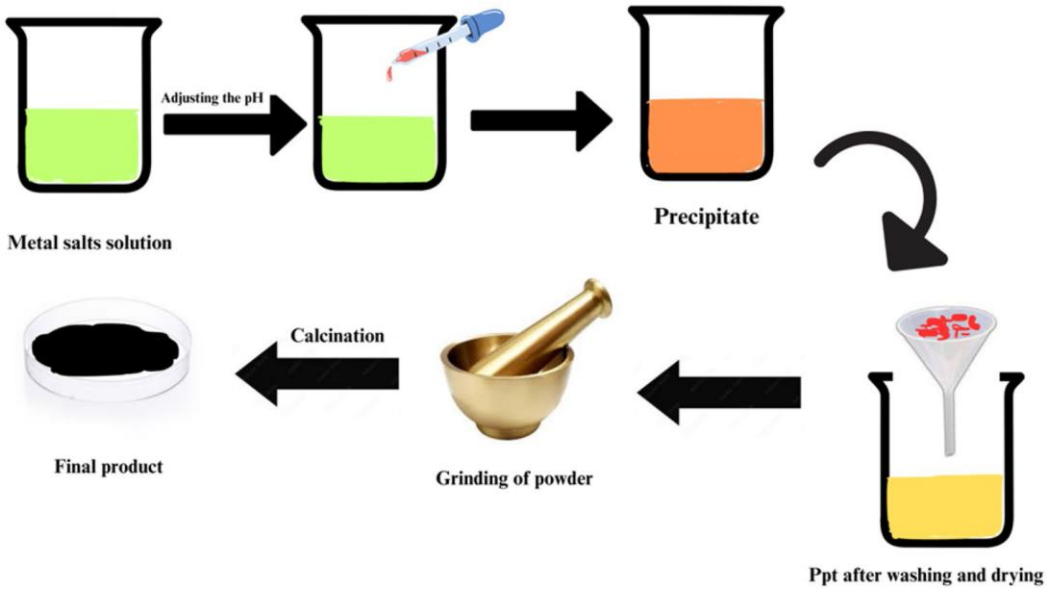


**Fig.II.1**: Representation of spinel ferrites synthesis by the coprecipitation method [10]

## II.2. Synthesis Precursors

### II.2.1. Hexahydrate Iron(III) chloride

Iron(III) chloride, either known as ferric chloride or iron perchloride, is an iron salt with the chemical formula $FeCl_3$. It is a compound that evolves vapors in humid air under the effect of hydrolysis. The dissolution reaction in water is very exothermic and forms a brownish acid solution. Its hexahydrate form or iron trichloride hexahydrate is yellow-brown or orange in color; it is the most common commercial form of ferric chloride. Its chemical formula is $FeCl_3*6H_2O$, it is a solid with a molar mass of 270,3g/mol, a melting point of 37°C, a boiling point (loss of water) of 280°C and a density of 1,82 at 25°C. This form is soluble in water, ethanol, diethyl ether and acetone. The hexahydrate and aqueous solutions split up at high temperature with the formation of hydrogen chloride [23,24].

### II.2.2. Hexahydrate Cobalt(II) chloride

Cobalt(II) chloride is a compound consisting of cobalt and chlorine, with the formula $CoCl_2$. It is usually found in the form of the hexahydrate $CoCl_2 \cdot 6H_2O$, which is the most commonly used cobalt compound. This hexahydrate form is purple.

In its solid state, it consists of one molecule of trans-$[CoCl_2(H_2O)_4]$ and two molecules of water of crystallization. The hexahydrate, with a molar mass of 237,93g/mol, a melting point of 87°C, and a density of 1,92, dissolves readily in water, ethanol, and acetone.

Aqueous solutions of $CoCl_2$ and its hydrate contain the species $[Co(H_2O)_6]^{+2}$, as well as chloride ions. These concentrated solutions are red at room temperature and turn blue when heated [23].

### II.2.3. Tetrahydrate Manganese(II) chloride

Manganese(II) chloride refers to a series of chemical compounds with the formula $MnCl_2(H_2O)_x$, where the value of x can be 0, 2, or 4. The tetrahydrate with the formula $MnCl_2 \cdot 4H_2O$ is the most common form of manganese(II) chloride. These salts are pink; the paleness of the color is characteristic of transition metal complexes with high-spin $d^5$ configurations. It is a paramagnetic salt [23].

## II.3. Techniques for characterizing spinel ferrite nanoparticles

### II.3.1. X-ray scattering

An ideal single crystal is a three-dimensional distribution of atoms that occupies all of space. Among the symmetry laws that enable this distribution, there is a translational symmetry that affords the crystalline structure its own periodic character. Since the crystals are randomly oriented that is the powder diffraction [11].

#### II.3.1.1. Geometric crystallography

Using a basis of three vectors $\vec{a}$, $\vec{b}$, $\vec{c}$ of $R^3$. The translation group generated by $(\vec{a}, \vec{b}, \vec{c})$ is the set of translations defined by the vectors:

$$\vec{t} = u\vec{a} + v\vec{b} + w\vec{c} \quad \text{with u, v, w relative integers} \qquad (2.1)$$

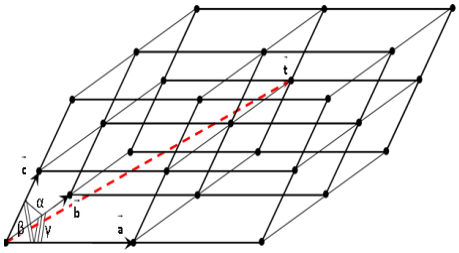


**Fig.II.2**: Node network [11]

If we draw all these vectors $\vec{t}$ from a common origin 0, their ends constitute a three-dimensional network of points. In crystallography, these points are named nodes. Three non-collinear nodes define a reticular plane. All the nodes are then distributed in a family of parallel planes equidistant from d (reticular distance). Each family of reticular planes is identified by its Miller indices, denoted (h k l), which are by definition, in the case of a primitive basis, whole numbers that are prime relative to each other (no common divisor). Two consecutive planes of the family are equidistant from $d_{hkl}$. In the case of a cubic system, the lattice parameter a and the distance $d_{hkl}$ are related by the relation [11]:

$$d_{hkl} = \frac{a}{\sqrt{h^2+k^2+l^2}} \qquad (2.2)$$

### II.3.1.2. Coherent X-ray scattering

For the diffusion of radiation by matter, we speak of the wavelength which is the basic criteria; it must be of the order of magnitude of the reticular distances of the crystal meshes (from a few tenths to a few ångström Å). According to their nature, we distinguish between electromagnetic radiation and corpuscular radiation.

As X-rays pass through matter, they undergo various types of interactions:

- the photoelectric effect: X-ray photons can act on the deep electron shells of atoms, causing them to transition from the ground state to an excited state by ejecting an electron. The ejected electron is called a photoelectron.
- elastic interaction or coherent scattering (Thomson scattering): the elastic interaction between the incident radiation and an atom as a whole does not occur and alters together the inner structure and the internal energy of the atom. The radiation having undergone this sort of interaction will be able to maintain its coherence. In the particular case of crystallized matter, this scattering of X-rays can give rise to interference phenomena (diffraction). This interaction is at the origin of X-rays scattering by matter. The survey of constructive interference of scattered waves is achieved in a simple geometric way. The relationships to scattered amplitudes are established within the framework of kinematic theory which assumes that the amplitude of the incident wave is constant at all points of the distribution of diffracting centers (no attenuation due to multiple scatterings).
- inelastic interaction or incoherent scattering (Compton effect): inelastic interaction takes place with one or more electrons of the atom. It modifies the internal structure, therefore the internal energy of the atom. The scattered radiation is no longer coherent and cannot initiate interference phenomena. Its interpretation calls upon the corpuscular aspect of electromagnetic radiation. During the collision with an electron, the X-ray photon loses only a small part of its energy. Its incident energy is found in two forms; part of the energy is conveyed to the electron (recoil electron) in the form of kinetic energy and the other part of the energy of a value lower than that of the incident is the energy of the

scattered, incoherent radiation. This is the Compton effect which is driven by the relativistic equations of conservation of energy and momentum. This scattering therefore not induces an increase in background noise [11].

### II.3.1.3. Intensity diffracted by a periodic structure, Bragg's law

Any crystal structure can be described from independent atomic positions (atoms A, B, C, D...) to which the translation lattice is applied.

The condition for constructive interference of waves scattered by a plane of atoms A parallel to the lattice plane (hkl) is $\Delta = n\,\lambda$ ($n \in Z$) such that $\Delta$ is the path difference of the radiation and $\lambda$ is the wavelength of the radiation from the source.

The condition for constructive interference of waves scattered by planes of atoms A equidistant from $d_{hkl}$ is $\Delta = 2d_{hkl}\sin\theta$ such that $\theta$ is the Bragg angle across the incident beam and the plane lattice. There will therefore be constructive interference for all A-type atoms in the structure if:

$$2\,d_{hkl}\,\sin\theta = n\,\lambda \quad \text{with } n \in Z_+^* \text{ is the interference order} \qquad (2.3)$$

This relationship is Bragg's law with $\lambda \leq 2d_{hkl}$. The intensity therefore has maxima in certain directions; we will disclose a diffraction phenomenon.

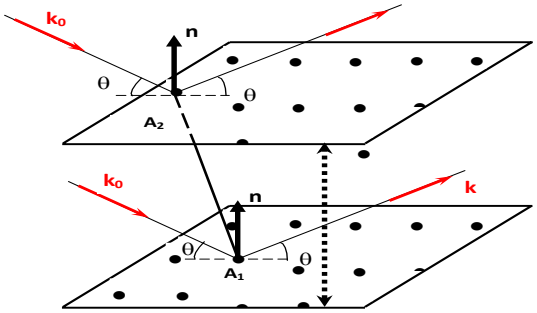


**Fig.II.3**: Scattered Waves by the planes of atoms [11]

There is also constructive interference for other atoms under the same Bragg conditions. It is said that we get the reflection on the plane (hkl) when the Bragg relation is satisfied. In practical crystallography, we no longer show interference order (diffraction order) and we use the Bragg relation in the form:

$$2\left(\frac{d_{hkl}}{n}\right)\sin\theta = 2\,d_{h'k'l'}\sin\theta = \lambda \qquad (2.4)$$

With: $h' = ph$, $k' = pk$, $l' = pl$ (Miller indices times the diffraction order) [11].

### II.3.1.4. The technical principle

Scattered X-rays are used to determine the crystallographic make up and microstructures of materials. XRD consists of drive on an angle of incidence $\theta$, a focused and monochromatic X-ray beam of wavelength $\lambda$ onto the crystalline material to be analyzed. Then, the detected intensity is recorded as a function of the deflection angle $2\theta$ of the X-ray beam, the resulting spectrum is called a diffractogram. In

a material, several frames can be present; for this reason, a fairly wide angular scan is carried out. The angles corresponding to the different diffraction peaks must check Bragg's law.

The intensity distribution around the diffraction position defines a diffraction peak. This distribution depends on the instrumental resolution of the diffractometer and the microstructure of the sample being studied. The curve that matches a peak is known as the line profile.

The $2\theta$ position is the angle at which the intensity is maximum for each peak in the diffractogram. The full width at half maximum (FWHM) is the angular distance between two points at which the intensity is half the maximum intensity.

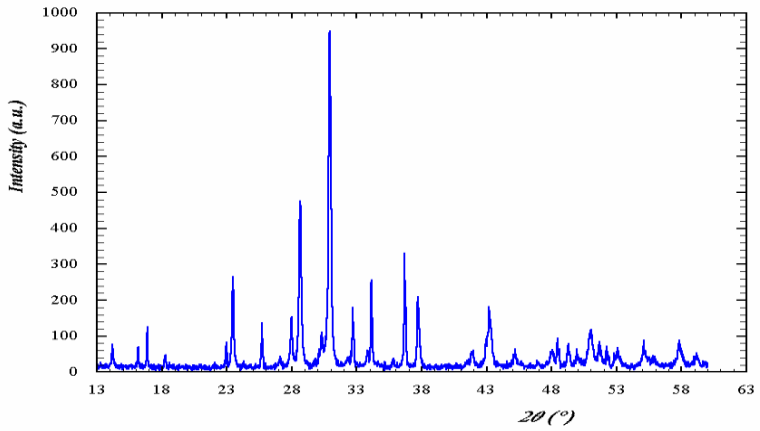


**Fig.II.4**: Experimental diffractogram of the isostructural compound [11]

The diffraction spectrum is specific and unique to a single phase, even if the phases have the same chemical composition. The identification of the phases is done by comparing experimental data to database records (JCPDS record), it is the search for compatible spectra in these databases.

### II.3.1.4.1. Phase search and selection

Nowadays, there are several methods for investigating X-ray scattering line profiles. Among the most widely used methods is the Scherrer-Wilson method. This method which is applied in X-ray scattering spectra adjustment software, and it is based on mathematical functions (Lorentzian, Gaussian, etc.) to describe accurately the X-ray line profile and perform a qualitative and quantitative analysis of a given material. HighScore Plus is also among the most widely used software.

Prior knowledge of the chemical elements present in the structure is necessary for the search and identification of crystalline phases. Spectrum analysis can sometimes be complicated due to peak shifts and the possibility of peak overlap, which may correspond to one or more phases [16].

### II.3.1.4.2. Computation of crystallite size

Matter is made up of a very large number of crystallites (monocrystals) with random orientations that is assumed to be perfectly statistical. Bragg's law was established by considering a small crystal (kinematic hypothesis), with a perfect translation lattice, placed in a beam of parallel X-rays assumed to be monochromatic.

In experimental practice, the diffracted intensity when passing to the Bragg condition is no longer recovered on a Dirac peak but on a diffraction line which has a certain angular width [11].

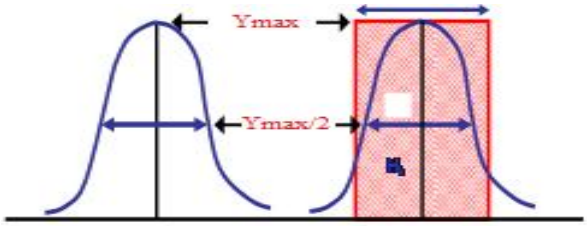


**Fig.II.5** : Diffraction line [11]

The area $S_{(hkl)}$ of the diffraction line is the integrated intensity of the reflection (hkl).

The reflective power P of the crystal is the ratio: $P = \frac{S}{I_0}$ ($I_0$ intensity of the incident radiation).

The width of the diffraction peaks is determined by:

- either the full width at half maximum $\Delta_k$, the index k denoting the k line.

$\Delta_k$ is a function of $2\theta$ and the Miller indices (crystallite shapes).

- or by the integral width $\beta_k$, defined as the width of the rectangle with the same height $y_{max}$ and the same area S as the peak: $\beta_k = \frac{S}{y_{max}}$ (fig.II.5)

A Gaussian diffraction peak is marked by its intensity (peak area), its angular position $2\theta$, and its full width at half maximum.

From an X-ray diffractogram, the average crystallite size $< D_{cris} >$ (or average size of the coherent diffraction domain, which is defined as the internal volume of the single crystal, excluding edge effects, and which allows constructive interference to be obtained) can be computed. Thus, it leads to a volume that is smaller than that of the single crystal. The Scherrer formula is expressed as:

$$D_{cris} = \frac{K\ \lambda}{\Delta(2\theta)\cos\theta} \qquad (2.5)$$

K : Scherrer constant whose value depends on the shape of the crystallites (generally close to 1).

$\Delta(2\theta) = \beta$ : width at half-maximum of the Bragg peak of maximum intensity (rad) [11].

### II.3.1.5. Principle of the X-ray diffractometer

X-rays have the property of travelling across a material and being diffracted by atoms, the degree of scattering depends on the energy of the incident radiation and the atomic distribution.

X-ray scattering makes it possible to ascertain the accurate distances $d_{hkl}$ between the different crystal planes (hkl) of a crystal, from the measurement of the deflection angles $2\theta$ of an incident X-ray beam. The measurements are carried out with a diffractometer which is made up of different elements. The device includes a high-voltage generator (60kV maximum, the maximum current value is 60 mA), an X-ray tube (anticathode copper, molybdenum, cobalt, etc.), a water cooler, a CCD detector and an electronic assembly responsible for controlling the goniometer and recording the diffractograms which represent the diffracted intensity I as a function of the angle $2\theta$.

The X-ray tube and the CCD detector arm on the goniometric head are rotated through an angle $\theta$ during acquisitions (Fig.II.7) [25].

The diffraction spectrum or diffractogram of the sample constitutes the characteristic fingerprint of the structure of the analyzed crystalline substances.

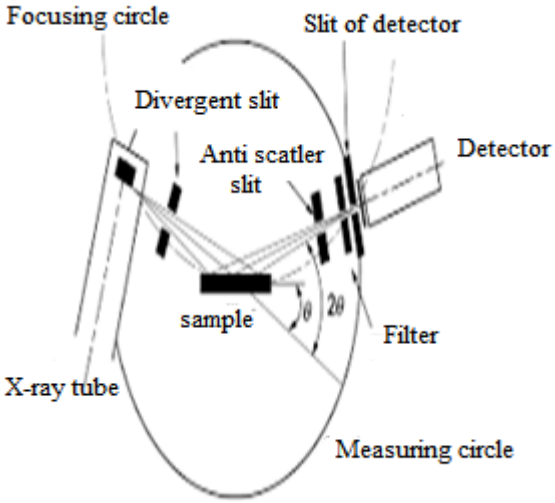


**Fig.II.6**: Diagram of the optical path of X-rays in goniometric mode [26]

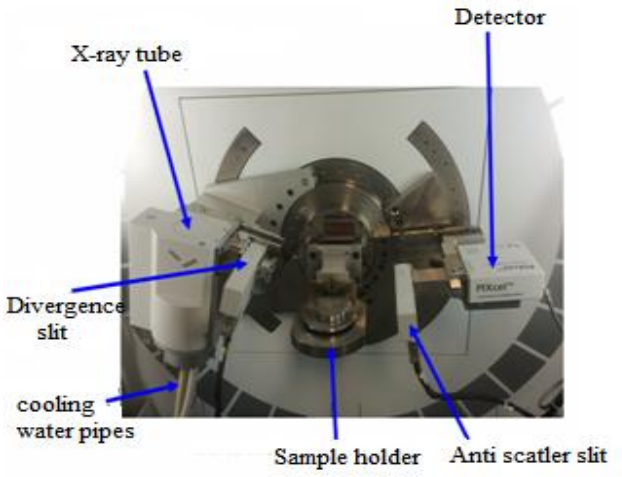


**Fig.II.7**: Detailed view of the sample holder and goniometric head with the RX tube, programmable slits and detector [25]

The diffractometer is set in an anti-vibration box with glass to block X-rays (which may be sent outside the detector). In addition, it is staged on a piece of granite to absorb external vibrations.

- X-ray tube :

Electrons torn from an electrically heated tungsten filament are accelerated under the effect of an intense electric field to bombard an anticathode (or anode) which can be of different nature depending on the intended applications. The two most commonly used metals in X-ray diffraction are copper ($\lambda = 1{,}54$ Å) and molybdenum ($\lambda = 0{,}709$ Å). For optimal diffraction, a wavelength of the same order of magnitude as the size of the grating must be used.

Since it is stroke by an electron beam, the anode will release most of the received energy in the form of heat, hence the use of a cooling circuit with water at a given pressure is necessary. A small portion will be in the form of X-rays.

These X-rays will travel in all directions, but the tube has apertures to the outside, and the rays will then be directed towards the monochromator.

- Monochromator :

The purpose of this optical device is to select a narrow band of wavelengths of radiation from a wider range of wavelengths. Filter is used to produce the monochromatic X-rays that are required to bring about scattering.

- Collimator :

The monochromator has generated a deviation of the X-ray beam. It will therefore be necessary to use a collimator to refocus the X-ray beam on the sample.

- The Goniometer Set :

The set consists of concentric circles whose positions can be adjusted till 1/1000th of a degree. This will allow the crystal to be aligned at any position.

- Detector :

It records diffraction images. A detector must have together higher quantum efficiency, better linearity, and more sufficient resolution. The efficiency (ratio of the number for detected particles to the number of received particles by the detector) depends on both the nature and energy of the radiation [25].

For diffractometers, several configurations are possible: Debye-Scherrer chamber, focusing chamber (Seeman-Bohlin and Guinier) and the Bragg-Brentano assembly.

- **Bragg-Brentano configuration** :

Type $\theta - \theta$, where the tube and detector move simultaneously at an angle $\theta$, the sample remains fixed. Type $\theta - 2\theta$, where the tube remains fixed, the sample and detector move respectively at an angle $\theta$ and an angle $2\theta$. Then, this purports that the planes that satisfy Bragg's law still parallel to the surface [27,16].

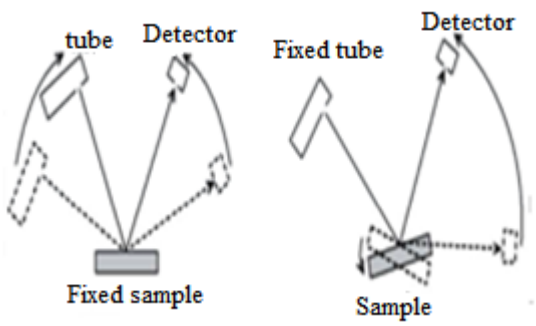


**Fig.II.8**: Operating models of diffractometers [16]

**Fig.II.9**: EMPYREAN Panalytical diffractometer (LM2S laboratory)

### II.3.2. Scanning electron microscopy

#### II.3.2.1. Technical Principle

Scanning electron microscopy is a powerful technique for observing the surface of samples, particularly the topography of unpolished surfaces. This technique is primarily based on the detection of secondary electrons emerging from the surface under the impact of a very fine beam of primary electrons that scans the observed surface. Thus, it grants images to be obtained with a spatial resolution often below 5 nm.

SEMs operate at high magnifications of up to 300000x or even 1000000x to produce highly accurate images of a wide range of materials. SEMs operate with generating an electron beam with much shorter wavelengths. The interactions of these electrons with the material often reflect the surface topography or composition, or even the local crystal orientation. These interactions result in different types of radiation, or particles, emanating from the bombarded sample:

- Secondary electrons provide morphological data on the specimen with a resolution of a few nanometers. They have low energy (around 50 eV) and are seized with the SED (Secondary Electron Detector). Secondary electrons are emitted in the surface layers close to the surface. Electrons that can be captured by detectors are often emitted at a depth of less than 10 nm. Then, due to this low kinetic energy, it is relatively easier to deflect them with a small potential difference and makes it easy to collect a large number of these electrons and reach high-quality images; meanwhile, secondary electrons also supply data on the topography of the sample.

- Backscattered electrons are generated from a deeper part of the sample will provide information on the heterogeneities of the sample composition, in other words will afford an image with chemical contrast on a surface. These electrons result the interaction of the electrons of the primary beam with the nuclei of atoms of the sample, this type of interaction is quasi-elastic. The electrons are re-emitted in a direction close to their original direction with lower energy loss.

  Hence, these recovered electrons have a relatively high energy of up to 30 KeV, the resolution is achieved with the backscattered electrons and will be somewhat low, i.e. in the order of a micrometer or a tenth of a micrometer. In addition, these electrons are sensitive to the atomic number of the atoms constituting the sample. The heaviest atoms will re-emit more electrons than the lighter atoms; areas formed by atoms with a high atomic number will appear brighter than others, so this is the phase contrast.

  These backscattered electrons are seized with a specific detector and will let a qualitative analysis.
- X-ray radiation from an even deeper region provides information about the chemical nature of the atom. When the atom is bombarded by a high-energy primary electron, an electron from a deeper layer can be ejected and the atom enters an excited state. De-excitation and filling of the energy order of the electronic structure occurs with X-ray emission. X-ray photons make possible chemical analysis in energy dispersive spectroscopy (EDS) that is a quantitative or qualitative analysis.
- Auger electrons: When an atom is excited by shelling de-excitation can occur by emitting an Auger electron (Auger effect). During de-excitation, an electron from a higher layer fills the gap created by the initially ejected electron. During this transition, the peripheral electron loses a certain energy which can be emitted in the form of an X-ray photon or can then be transmitted to an electron from a more external and therefore less energetic orbit. This peripheral electron is in turn ejected and can be recovered by a detector [28,29].

**Fig.II.10**: Scanning electron microscope [30]

### II.3.2.2. Operating principle of the scanning electron microscope

The instrument allows the formation of a very fine beam (down to a nanometer) of electrons accelerated with an adjustable voltages from 0,01 to 30 kV, to focus and to scan it over the area of the surveyed sample. The SEM is essentially consists of the upcoming elements:

- an electron gun: the electron probe is a beam of electrons, it is thinner and produced by an electron gun which acts as a source that is lowered with electronic lenses.
- coils: arranged along the two axis perpendicular to the beam axis and are crossed by synchronized currents, they allow the probe to be submitted to scanning.
- electromagnetic lenses.
- an electron column: the magnetic lenses and scanning coils form an assembly called the electron column. The function of this element is to produce a fine electron probe on the sample.
- a specimen stage allowing the specimen to shift in three directions.
- electron detectors: they are specific sensors (secondary, backscattered, X-ray, etc.) supplemented by photon detectors, or others, making it possible to collect significant signals emitted during scanning of the surface, and to form various images then synchronized with the scanning.
- a vacuum pump: the device must necessarily be equipped with a vacuum pump system [28,29].

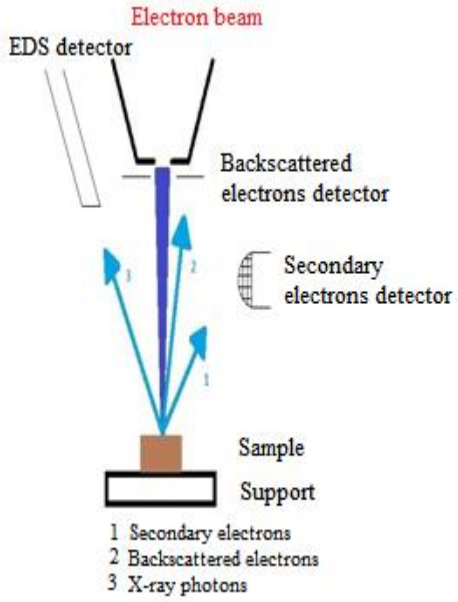


**Fig.II.11**: Different types of radiation from the shelled sample [31]

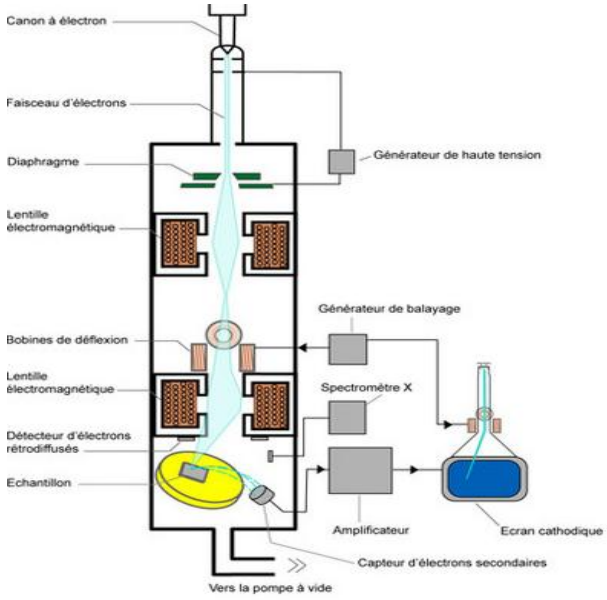


**Fig.II.12**: Schematic representation of the SEM [32]

### II.3.2.3. Different types of imaging

An electron sensor displays the flow of electrons into brightness on a screen. By a survey of the surface, discrepancies in contrast are detected, creating a relief-like image of the surface. The black and white colors in the resulting micrograph are a reproduction with an electronic system.

- Secondary electron imaging: this is a portrayal of the surface morphology. In reality, the amount of secondary electrons that is produced not depends on the chemical nature of the sample, but on the angle of incidence of the primary beam with the surface. More is grazing the incidence, the larger is the excited volume, therefore greater the production of secondary electronsis resulting in a topographic contrast effect (a slope appears brighter than a flat one).
- Backscattered electron imaging: we therefore obtain a chemical contrast, the areas containing light atoms appearing darker.
- Backscattered electron diffraction imaging: it leads the orientation of the different grains in a polycrystalline material to be determined and the phases of a crystallite to be identified, the composition of which has previously been achieved by means of X-ray spectrometry.
- Elemental chemical imaging via X-ray spectrometry: by analyzing the X-ray spectrum, one can have a chief analysis, i.e. to perceive the type of nearby atoms, and even draw up a chemical framework. The analysis can be done with wavelength dispersive spectroscopy (WDS) or by energy selection (EDS). The technique using wavelengths is more accurate and enables quantitative analyses, while using energy is faster and less expensive.

### II.3.3. Vibrating sample magnetometry

#### II.3.3.1. Technical Principle

Vibrating sample magnetometry is mainly a technique for characterizing the magnetic features for powders.

A Vibrating Sample Magnetometer measures magnetization as a function of the applied static magnetic field. The material is placed at the center of an electromagnet that can provide a magnetic field of up to 2 Tesla. Then, the sample is carried by a rod, vibrates vertically across a transducer. The vibration movement is set apart by an amplitude and a vibration frequency. The electromechanical system is fixed on pads integral with the magnet so that the specimen stands at the center of the pole pieces in an area where the field is perfectly homogeneous. Two pairs of detector coils are held fixed on the pole pieces of the electromagnet. The vibration motion of the magnetized material in this area generates a variation in the magnetic flux across the effective cross-section of the detector coils, giving rise to an induced electromotive force (EMF). According to Lenz's law, the potential difference measured across the terminals of the detector coils is proportional to the flux variation.

$$e = -\frac{d\Phi}{dt} \qquad (2.6)$$

This magnetic flux is proportional to the magnetic momentum of the sample. Since the measured voltages are generally lower, the signal related to the magnetic sample is then detected and amplified. An advanced software grants the user to set several parameters such as the acquisition time, the sampling step and the applied limit field. The VSM allows the simultaneous measurement of the longitudinal and

transverse components, respectively parallel and perpendicular to the applied field via using two sets of coils. From these measurements, it is possible to study the processes that are involved in both reversal and in particular magnetization to discern a difference for the reversal magnetization modes. Figure II.15 shows a hysteresis cycle measured using the VSM for a magnetized sample.

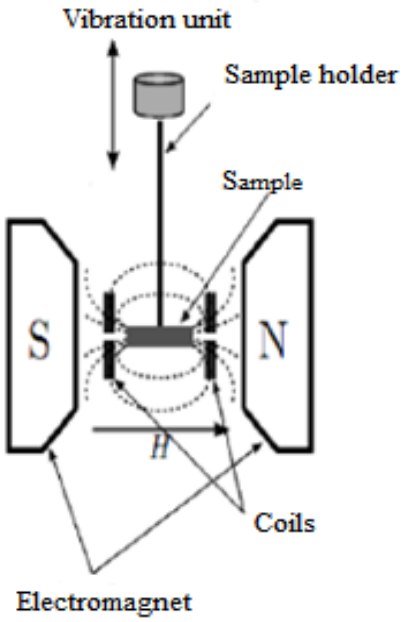


**Fig.II.13**: Diagram of the VSM device [16]

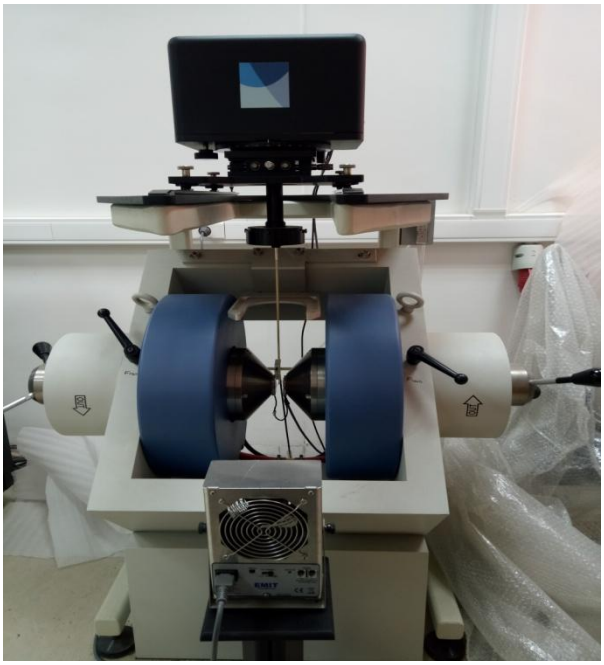

**Fig.II.14**: VSM Overview (LM2S laboratory)

The longitudinal and transverse components lead to various physical quantities, so the resulting parameters from the increasing and decreasing in field branches are followed by an exponent + and - respectively. The parameters are $M_S$, $H_C$, $M_r$ et $M_t$.

$M_S$ is the saturation magnetization which is proper to the maximum magnetization of the sample where all the magnetic momentum are aligned in the same direction.

$H_C = \frac{H_C^+ - H_C^-}{2}$ is the coercive field which corresponds to the field that must be provided to have zero magnetization.

$M_r = \frac{M_r^+ - M_r^-}{2}$ is the remanent magnetization corresponds to the value of the magnetization at nonattendance field for the longitudinal components.

$M_t = \frac{M_t^+ - M_t^-}{2}$ is the maximum transverse magnetization (in the case of transverse components). $M_t^+$ and $M_t^-$ are the positions of the main peak at each branch. Note that the reversal is said to be coherent when $M_t/M_S$ is 1. Otherwise the reversal is said to be incoherent [33].

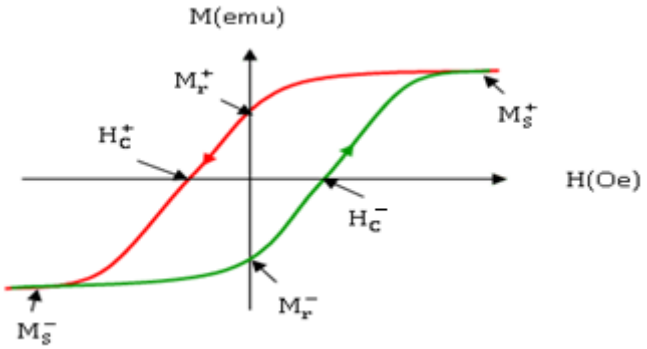


**Fig.II.15**: Hysteresis cycle

### II.3.3.2. Measurement setups

Two configurations are possible in the VSM:

- In-plane configuration: the applied magnetic field is parallel to the specimen; in this case the deposition axis as well as the easy axis of magnetization are in the plane. By rotating the sample, an in-plane magnetic anisotropy can be displayed by means of this array.
- Out-of-plane configuration: the magnetic field is perpendicular to the sample. The magnetization is in a perpendicular plane [33].

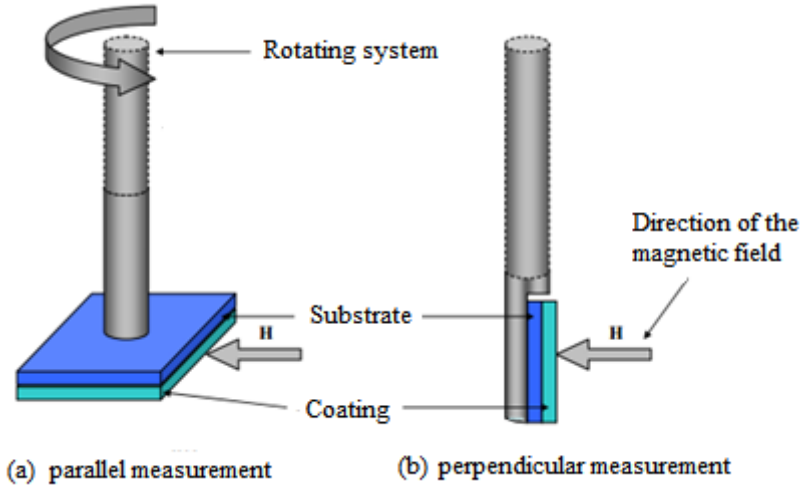


**Fig.II.16**: Possible configurations (parallel and perpendicular) in the VSM [33]

Magnetization plots can be recorded in two configurations, the parallel configuration and the perpendicular configuration.

# Chapter III

## Results and discussions

In this section is mostly devoted to reveal in more details the synthesis method of manganese-cobalt spinel ferrite nanoparticles $Mn_{0,5}Co_{0,5}Fe_2O_4$. The development process is inspired from some research work on spinel ferrite nanoparticles [34], [35], [36], [37], [38], [39], [40], [41]. Then, we state the different structural, microstructural and magnetic properties of these nanoparticles that are synthesized along the coprecipitation method. Indeed, three characterization techniques are wielded namely X-ray diffraction, scanning electron microscopy and vibrating sample magnetometry.

Finally, the last part of this chapter is focused on the applications of nanometric spinel oxides.

## III.1. Synthesis of spinel ferrite powders

One reach nanoparticles of homogeneous size and shape within the following synthesis protocol is followed:

### III.1.1. Cleaning the beakers

The beakers are cleaned with distilled water and acetone.

### III.1.2. Preparation of homogeneous solutions

The precursors are based on iron (III) chloride hexahydrate ($FeCl_3*6H_2O$), cobalt (II) chloride hexahydrate ($CoCl_2*6H_2O$) and manganese (II) chloride tetrahydrate ($MnCl_2*4H_2O$). Then agent responsible for the coprecipitation is clearly sodium hydroxide (NaOH).

Three separate solutions have been prepared:

- The $Fe^{+3}$ solution is prepared by dissolving 6,9717g of $FeCl_3*6H_2O$ in 50ml of distilled water.
- The $Co^{+2}$ solution is made ready by dissolving 1,5342g of $CoCl_2*6H_2O$ in 50ml of distilled water.
- The $Mn^{+2}$ solution is get ready by dissolving 1,2761g of $MnCl_2*4H_2O$ in 50ml of distilled water.
- A fourth sodium hydroxide solution is prepared by dissolving 4,1265g of NaOH in 100ml of distilled water.

**Fig.III.1**: Iron (III) chloride hexahydrate

**Fig.III.2**: Cobalt (II) chloride hexahydrate

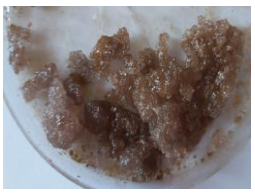

**Fig.III.3**: Manganese (II) chloride tetrahydrate

**Fig.III.4**: Sodium hydroxide

The homogenization step is carried out by magnetic stirring at a selected temperature. To do this, a magnetic bar (Fig.III.5) is placed in each beaker containing a non-homogeneous solution of metal ion salt and then all the beakers are placed on the heating plate (Fig.III.6). The heating magnetic stirrer allows the

stirring speed to be adjusted to 400 rpm (knob on the right) and the heating temperature to 80°C (knob on the left) and the stirring time is 15 min.

**Fig.III.5**: Magnetic bar


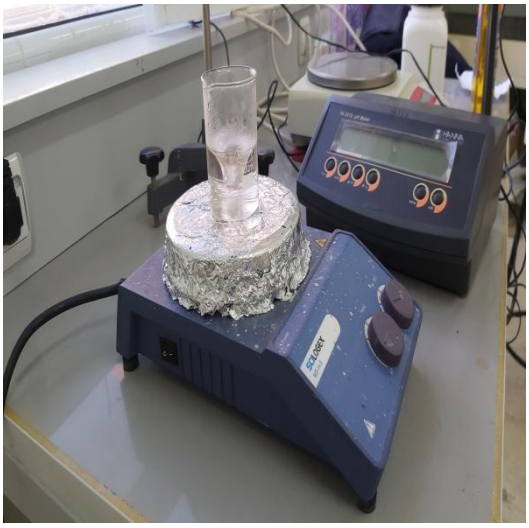

**Fig.III.6**: Solutions homogenization

### III.1.3. Mixing solutions

The $Fe^{+3}$, $Co^{+2}$ and $Mn^{+2}$ solutions are mixed in a single beaker which is put down on the hotplate. This reaction medium is then heated to a temperature of 80°C under magnetic stirring. All together, the sodium hydroxide solution is added dropwise to the mixture of three solutions. The basicity of the solution was buffered at pH = 10 (Fig.III.7) and the stirring is maintained for 10 min. After this time, a brownish precipitate is formed. Thus this color indicates the formation of the manganese-cobalt ferrite phase.

### III.1.4. Filtering and rinsing

Subsequent to synthesis and in order to obtain a solution at neutral pH, the precipitate is rinsed several times with distilled water and filtered to be finally be dried and in this step, a filter paper and a beaker are used (Fig.III.8). The purpose of this step is to remove salts and excess base in the medium. Later, the beaker is left for 48 hours.

### III.1.5. Drying and grinding

The precipitate was dried at 102°C for 3 hours in an oven (Fig.III.9). Therefore to ensure that this synthetic product is completely dry, a glass desiccator is also used to remove moisture from the substance (Fig.III.11).

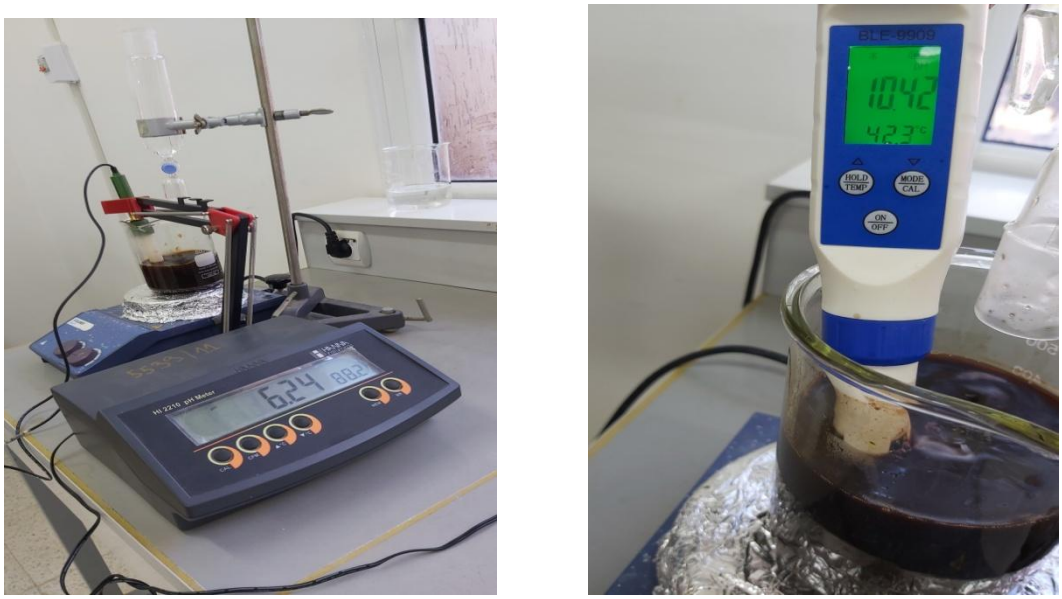

**Fig.III.7**: Experimental device

**Fig.III.8**: Solution filtering

With use of a wooden spatula, the substance is placed in a ceramic mortar to be ground and finely milled. Before grinding, the walls of the mortar must be thoroughly cleaned with sulfuric acid ($H_2SO_4$), then with a detergent, and finally rinsed with petroleum ether.

After grinding, the manganese-cobalt ferrite powders are obtained, but additional heat processing is necessary make certain that the nanoparticles are properly crystallized.

**Fig.III.9**: Stove

**Fig.III.10**: The resulting substance after drying at 102°C

**Fig.III.11**: Desiccator


**Fig.III.12**: Ceramic mortar

### III.1.6. Ashing at 600°C

The resulting powder is ashed at 600°C for 6 hours in a furnace, the aim of which is to improve the crystallinity of the ferrites.

**Fig.III.13**: Oven

**Fig.III.14**: Manganese-cobalt spinel ferrite powder

## III.2. Characterization of $Mn_{0.5}Co_{0.5}Fe_2O_4$ nanoparticles

### III.2.1. X-ray diffraction characterization

X-ray diffraction is a qualitative and quantitative analysis method. This technique depends on the analysis of diffractograms. The positions of the lines drives to the identification of crystalline phases and the computation of its lattice parameters. The shape of the lines provides information on the size of the coherent diffraction domains and on the rate of structural defects inherent this material.

The relative intensities of the lines make it possible to trace the position of the different atoms in the crystalline lattice.

### III.2.1.1. Analysis of X-ray diffraction spectra

The diffractogram of the prepared $Mn_{0,5}Co_{0,5}Fe_2O_4$ nanoparticles is shown in Figure III.15. X-ray scattering analysis is performed with an EMPYREAN Panalytical diffractometer, with the $2\theta$ angle ranging from 10° to 100° with a step size of 0,0133. Then, the source wavelength is $\lambda = 1{,}5406$Å of the $K_{\alpha 1}$ line of copper.

Phase identification of the sample has been fulfilled by comparing the experimental diagram with the reference diagrams in the JCPDS (Joint Committee on Powder Diffraction Standards) file. This is a database integrated into the High Score Plus software.

According to the diffractogram that is shown beneath, two crystalline phases have been detected; a main phase and a secondary phase.

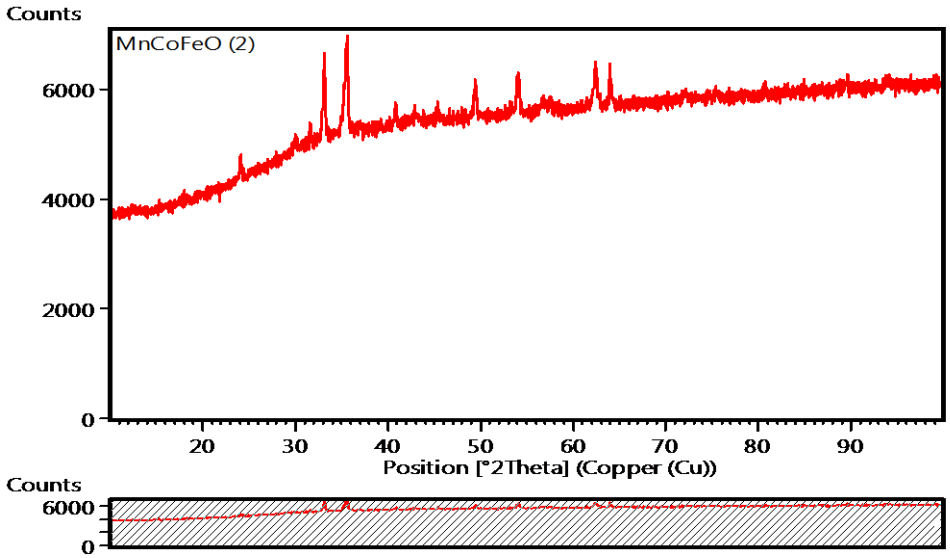


**Fig.III.15**: Diffractogram of $Mn_{0,5}Co_{0,5}Fe_2O_4$ nanoparticles

The experimental diffraction peaks of the main phase match to the peaks for a cubic structure. Thus, the most intense lines at $2\theta$ = 35,438°, 62,587°, 56,975° and 30,085° correspond respectively to the reflection planes (113), (044), (115) and (022) which are attributed to the cubic structure of cobalt spinel ferrites $CoFe_2O_4$ (JCPDS sheet n°00-022-1086) and are belonging to the space group Fd-3m (n° 227 in the international tables). The crystal lattice parameter is a = 8,3919Å.

Each diffraction peak profile has a well-defined crystallinity order belonging to the studied material.

Furthermore, it is noticed that the diffractogram presents a hump which is most likely explained by an insufficient ashing time, this is the time after which the ferrites become spinel type with a high degree of crystallinity.

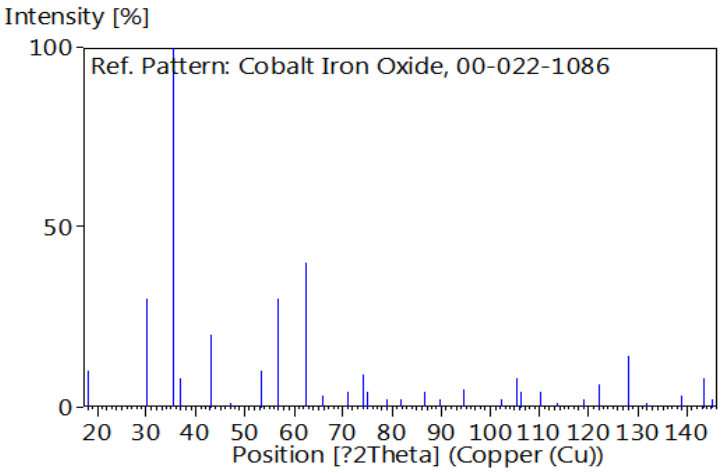


**Fig.III.16**: Stick Pattern

As shown in Figure III.15, the angular positions $2\theta$ = 33,157°, 35,632°, 54,068°, 49,463°, 24,149° and 62,438° characterize the peaks of a secondary phase with a rhombohedral structure are belonging to the space group R-3c and with the chemical formula $Fe_2O_3$ which is obviously hematite. The appearance of this phase is due to several factors, namely the composition of the precursors, impurities from grinding, heat treatment and or sometimes the environment surrounding the reaction medium.

The obtained results are clearly in agreement with other published works on spinel ferrites [37], [42], [39] and more particularly on manganese-cobalt spinel ferrites [43].

### III.2.1.2. Crystallite size

The crystallite size of the nanopowders is calculated for all diffraction peaks using the Scherrer formula; the average size $D_{cris}$ calculated is approximately 40 nm.

The width at half maximum is trivial and presents an ideal crystalline coherence while the spectrum has a Dirac shape. On the other hand, increasing this width reduces this coherence and the material studied is amorphous which has a Gaussian shape spectrum.

In fact, the crystalline phase and crystallite size of NPs are the parameters that bias their activity and properties [40].

### III.2.2. SEM-EDS characterization of nanoparticles

Scanning electron microscopy is combined with energy-dispersive X-ray spectroscopy to assess the surface morphology and elemental compositions of the nanoparticles.

The sample surface is examined by means of a SEM. Then, images of the synthesized nanoparticles at the nanoscale are shown in figure III.17. Thus, particles with roughly spherical shapes are observed at the nanoscale. The sizes of the nanoparticles are measured and the mean size is around 60 nm. Due to

magnetic force, crystallite agglomeration results in a non-uniform and heterogeneous distribution of nanoparticles.

Later on, the mean value for crystallite size of spinel ferrites obtained from the XRD diagram are close to slightly tiny than that of the average size for nanoparticles which are obtained with SEM.

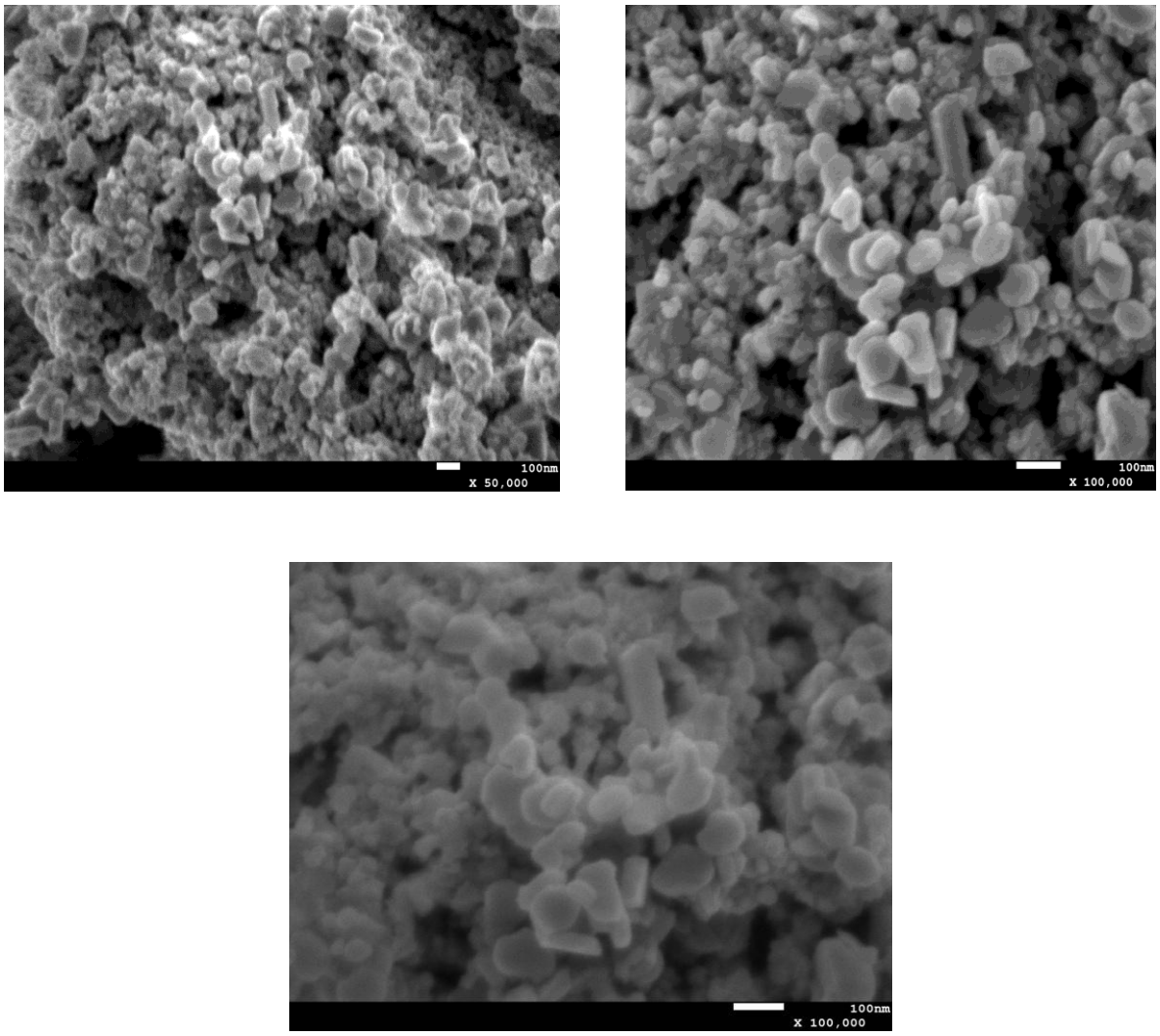


**Fig.III.17**: SEM micrographs of $Mn_{0,5}Co_{0,5}Fe_2O_4$ nanoparticles

EDS spectroscopy leads to the local determination of the elemental chemical composition of a scanned medium by SEMs so, the EDS spectrum is illustrated in figure III.18.

EDS analysis is implemented to fullfill a quantitative study of the present elements, and scanning with a probe provides a chemical map of the area considered, also an image that enables a better visualization of the morphological characteristics of the nanoparticles is presented in figure III.19.

In fact, the resulting nanoparticles must contain only the iron, oxygen, cobalt and manganese and no other impurities should appear, however according to the EDS spectrum, a carbon element is noticeable, this is due to the presence of higher level of carbon particles indoors the laboratory. Therefore, the EDS measurements are altered by the carbon element what so it is unavoidable in the spectrum. In addition, the

appearance of chlorine and sodium particles at lower ratios is due to salt residues. Rinsing several times is necessarily and drives to remove them.

The different mass and atomic ratios of the chemical elements which are deduced from the EDS spectra are reported in Table III.1.

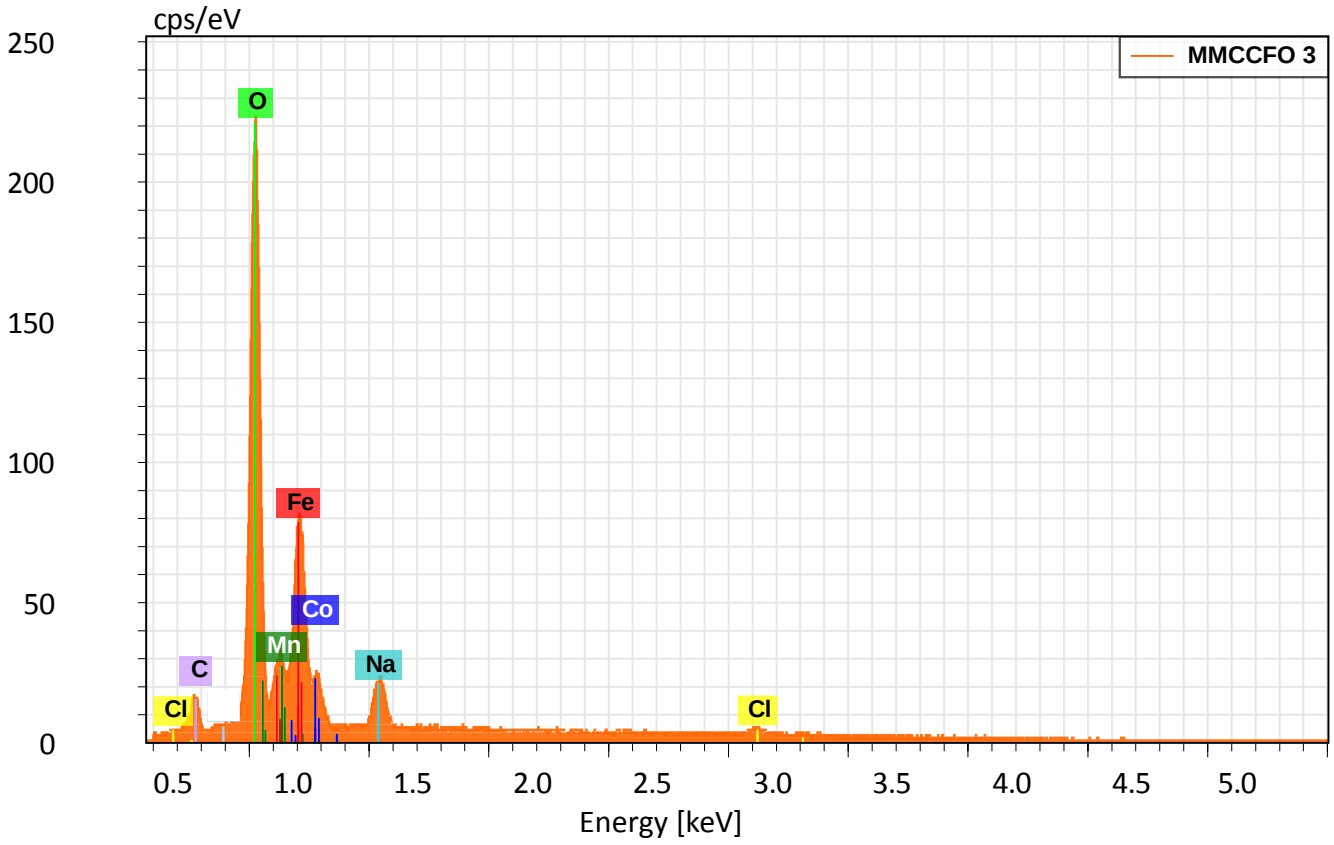


**Fig.III.18**: EDS spectrum for $Mn_{0,5}Co_{0,5}Fe_2O_4$ nanoparticles

| Element | At.No. | Mass [%] | MassNorm. [%] | Atom [%] |
|---|---|---|---|---|
| Iron | 26 | 42.93 | 42.93 | 20.66 |
| Oxygen | 8 | 37.59 | 37.59 | 63.16 |
| Manganese | 25 | 5.52 | 5.52 | 2.70 |
| Cobalt | 27 | 5.29 | 5.29 | 2.41 |
| Sodium | 11 | 4.72 | 4.72 | 5.52 |
| Chlorine | 17 | 2.24 | 2.24 | 1.70 |
| Carbon | 6 | 1.71 | 1.71 | 3.84 |
| | | **100.00** | **100.00** | **100.00** |

**Tableau III.1**: Different mass and atomic ratios of chemical elements

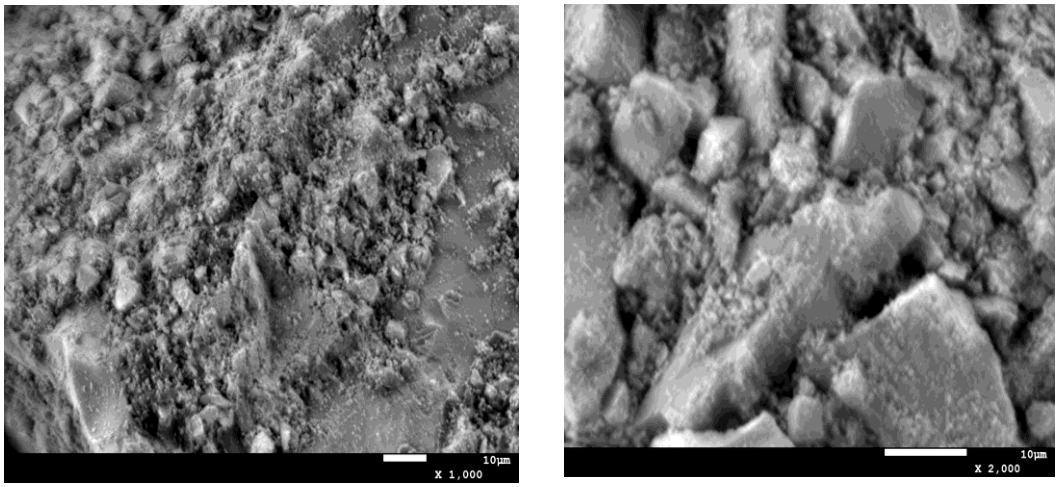


**Fig.III.19**: EDS image of $Mn_{0,5}Co_{0,5}Fe_2O_4$ nanoparticles

### III.2.3. Magnetic properties of nanoparticles

#### III.2.3.1. Hysteresis curve

The magnetic analysis is performed with using a vibrating sample magnetometer at room temperature. Then, one reach better results for the sample's hysteresis loop while the external magnetic field G is varied within two extreme values, -10 kOe and +10 kOe. For that reason, external magnetic field till to 10 kOe in parallel and perpendicular to the sample is applied. Magnetic measurements are achieved with a VSM and enable to obtain hysteresis loops that represent the variations in the magnetic moment/mass (emu/g) versus the applied magnetic field G(Oe). Figure III.20 shows the behaviour for the magnetization against the magnetic field, and the resulting hysteresis confirm that the sample belongs to the family of soft ferromagnetic materials.

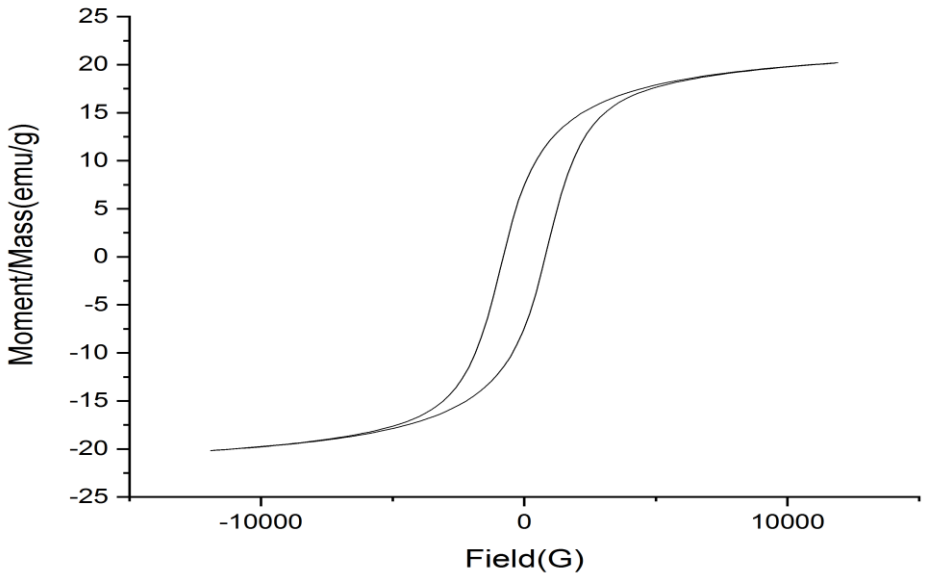


**Fig.III.20**: Magnetization cycle for nanoparticles

Whereas an external magnetic field is applied to a ferromagnetic material, the magnetic area gradually follow the direction of the field and for soft magnetic materials the magnetization aligns easily in the presence of the field. The hysteresis loops of these materials are narrow and quickly saturated, as a result the coercive fields are weak (<1000A/m). Generally, these materials have high positive magnetic susceptibilities and are temperature-dependent. In addition, they are characterized by high permeability. In cases where the magnetization requires a stronger field for alignment, the material is considered a hard ferromagnet, so the hysteresis loops of these materials are wider with high coercive fields [33].

### III.2.3.2. Magnetic properties

A ferromagnetic substance has a non-zero resulting magnetic moment even in the absence of an applied magnetic field, i.e., a spontaneous magnetization M. Then, from the magnetization curve, one can deduce the values for the magnetic properties characterizing the synthesized NPs.

- saturation magnetization:

$M_S^+ = 20.197$ emu/g, $M_S^- = -20.172$ emu/g

- remanent magnetization: this is the natural amount expressing the fact that a ferromagnetic material can be spontaneously magnetized even in the absence of an external field.

$M_r^+ = 7.4670$ emu/g, $M_r^- = -7.4155$ emu/g

- Coercive field: this is the field that must be applied to reduce the remanence magnetization to zero. On the other hand, it is the field that must be applied to reverse the magnetization direction of a ferromagnetic material.

$H_C^+ = 791.97$ Oe, $H_C^- = -799.32$ Oe

- The cycle area: the surface area of a hysteresis cycle represents the energy that is exhausted per volume unit of the ferromagnetic material in order to reorient the magnetic moments of the domains and move the Bloch walls during a complete cycle of external magnetic field variation [16].

In closing, the results in this section emphasize to study the properties of manganese cobalt nanoferrites that are synthesized by coprecipitation; then, one has focused as well on the identification of the cubic spinel phase, as on the chemical composition of the nanoparticles, with compromise to the mass and atomic ratio of the chemical elements. As a consequence, magnetization curve has showed that the sample has a behavior of a ferromagnetic material whose SEM have disclosed the morphology of its nanometric size particles.

# Conclusion

In this work, we are primarily engrossed in the synthesis of manganese-cobalt spinel ferrite nanoparticles $Mn_{0,5}Co_{0,5}Fe_2O_4$, and in the second place, one investigate together their structural, microstructural and magnetic properties. For this purpose, a more customary synthesis method has been adopted which is coprecipitation.

Indeed, the characteristics for these spinel structure metal oxides depend on the distribution of metal ions on the crystallographic sites of the two tetrahedral and octahedral sublattices, in turn the distribution of ions steadily depends on the chosen synthesis route, the heat treatment that the sample undergoes but especially the cooling conditions after ashing. Whilst, the main difficulty in interpreting the results of ferrite analysis comes precisely from their crystallographic composition, the cationic distribution is also influenced by various parameters such as the ionic radius of the cations, the stabilization energy in the crystal field and the electronic configuration.

Further, several factors can influence the rate of formation and stability of precipitates formed during the coprecipitation process and consequently the shape, size and chemical composition. Parameters such as pH value, concentration of metal salts, synthesis temperature and the nature of the base used can be stated.

The obtained nanoferrite powder has been conjointly characterized by X-ray scattering, scanning electron microscopy coupled with EDS analysis and vibrating sample magnetometry.

First, X-ray analysis enables to check the crystallinity of the NPs, the purity of the phase and to give the limiting size of the crystallized coherent area by the width of the diffraction peaks. Then, the results have revealed the presence of two crystalline phases namely, a main phase with a cubic structure characteristic for spinel that is attributed to cobalt spinel ferrites, and another secondary phase which is attributed to hematite. The appearance of this last phase can be set forth by the influence of certain factors during the elaboration process, i.e. the precursors composition, the scanty cleaned beakers, the heat treatment or sometimes the environment surrounding the reaction medium. Under the experimental conditions used, the mean size of the crystallites computed from the X-ray diffractogram is in the range of 40nm.

Hereafter, SEM analysis lead to accurately determine the nanoparticles morphology whose sizes are greater than 40nm. Then, crystallite average size calculated by XRD is slightly smaller than that of the investigated nanoparticles by SEM, in reality, the images has obviously shown a non uniform size distribution of the nanoparticles which had quasi-spherical shapes with slight agglomeration due to their nanometric size. Later, EDS analysis has confirmed the presence of all the chemical elements in the synthesized nanoferrite.

Furthermore, the magnetic properties of the crystallized powder are considerate to emphasize ferromagnetic behavior.

At length, a further study is essential to investigate the exact cationic distribution on the octahedral and tetrahedral sites. This study will allow us to better understand the electrical and magnetic behaviors of these nanoparticles and to open up new fields of application for these nanomaterials.

# References


**[1]** Ala Manohar et al., Structural and electrochemical properties of mixed calcium-zinc spinel ferrites nanoparticles, Ceramics International, Vol. 49 (3), 4365-43711, 2023

**[2]** Shameran Jamal Salih, Wali M. Mahmood, Review on magnetic spinel ferrite ($MFe_2O_4$) nanoparticles: From synthesis to application, Heliyon, Vol. 9, e16601, 2023

**[3]** Véronica Gavrilov-Isaac, Synthèse de nanoparticules magnétiques à énergie d'anisotropie modulable, Thèse de Doctorat, Paris 6 University, 2015

**[4]** Touahri Souad, propriétés magnétiques des deux composes spinelle $Cu_{1.05}Cr_{1.05}Zr_{0.95}Se_4$, Mémoire de Master, Kasdi Merbah University-Ouargla, 2015

**[5]** Bawoke Mekuye, Birhanu Abera, Nanomaterials: An overview of synthesis, classification, characterization, and applications, Nano Select, Vol. 4 (8), 486-501, 2023

**[6]** G. Chuto, P. Chaumet-Riffaud, et le Groupe Oncologie de la Société française de médecine nucléaire et imagerie moléculaire (SFMN), Les nanoparticules, Médecine Nucléaire, Vol. 34 (6), 370-376, 2010

**[7]** Nadeem Joudeh , Dirk Linke, Nanoparticle classification, physicochemical properties, characterization, and applications: a comprehensive review for biologists, Journal of Nanobiotechnology Vol. 20, N°262, 2022

**[8]** Prathamesh R. Sune, Kajal S. Jumde, Pooja R. Hatwar, Ravindra L. Bakal, Samiksha D. More and Atharv V. Korde, Nanoparticles: Classification, types and applications: A comprehensive review, GSC Biological and Pharmaceutical Sciences, Vol. 29(03), 190-197, 2024

**[9]** Hebbal Elhadja, Synthèse et caractérisations électriques et optiques de phases de type spinelle, Mémoire de Master, Ibn Khaldoun University-Tiaret, 2015

**[10]** Shayista Gaffar, Amit Kumar, Ufana Riaz, Synthesis techniques and advanced applications of spinel ferrites: A short review, Journal of Electroceramics, Vol. 51, 246–257, 2023

**[11]** Pierre Gravereau, Introduction à la pratique de la diffraction des rayons X par les poudres, 3rd cycle. Diffraction des rayons X par les poudres, Bordeaux 1 University, France, pp.209, 2011

**[12]** Kaid Hamza, Kerdouci Ilham, Traitement des effluents de la tannerie « ACED » de Rouiba : Adsorption /photoréduction du Cr(VI) en Cr(III) sur les ferrites de type spinelles, Mémoire de Master, Abou-Bekr Belkaid University-Tlemcen, 2023

**[13]** Mehdi Ammar, Étude du magnétisme de composites métal-oxyde et métal-diélectrique nanostructurés pour composants passifs intégrés, Thèse de Doctorat, École normale supérieure de Cachan - ENS Cachan, 2007

**[14]** Sahnoune Derradji, Etude de l'influence des conditions de synthèse sur les propriétés des oxydes de la structure spinelle $NiFe_2O_4$, Mémoire de Magister, Mohamed Kheider University-Biskra, 2015

**[15]** Lilia Ajroudi, Ferrites de cobalt nanostructurés ; élaboration, caractérisation, propriétés catalytiques, électriques et magnétiques, Thèse de Doctorat, Toulon University; Tunis University, 2011

**[16]** Lamine Taberkani, Elaboration et investigation de propriétés structurales, électriques et magnétiques de couches minces ferromagnétiques de $Fe_x$ $Ni_{100-x}$, Thèse de Doctorat, Ferhat Abbas University-Sétif 1, 2023

**[17]** Henrik L. Andersen et al., The Chemistry of Spinel Ferrite Nanoparticle Nucleation, Crystallization, and Growth, ACS Nano, Vol. 18 (14), 2024

**[18]** Sanjeet Kumar Paswan et al., Spinel Ferrite Magnetic Nanoparticles. An Alternative for Wastewater Treatment, Chap. 11, 2021

**[19]** Sareh Mosleh-Shirazi et al., Investigation through the anticancer properties of green synthesized spinel ferrite nanoparticles in present and absent of laser photothermal effect, Ceramics International, Vol. 49 (7), 11293-11301, 2023

**[20]** Akila Benmeghazi, Khaldia Chaa, Etude photocatalytique de décoloration du colorant AG25 par l'utilisation des nanoferrites, Mémoire de master, Mostaganem University, 2023

**[21]** Zelin Li et al., An Overview of Synthesis and Structural Regulation of Magnetic Nanomaterials Prepared by Chemical Coprecipitation, Metals, Vol. 13 (1), 152, 2023

**[22]** Mohamed Alae Ait Kerroum, Synthèse et fonctionnalisation de nano-ferrites pour le traitement par hyperthermie, Thèse de Doctorat, Strasbourg University, 2019

**[23]** https://fr.wikipedia.org/wiki/Chlorure_de_fer(III)

**[24]** Base de données Fiches toxicologiques, Trichlorure de fer Fiche toxicologique n°154, inrs, Edition Février 2021

**[25]** https://lise.upmc.fr/diffractionx

**[26]** Kostiantyn Tabalaiev, Etude de la structure et des propriétés de l'acier à béton après déformation à froid, Thèse de Doctorat, l'école centrale de Lyon, 2010

**[27]** Bouchrit Souhila, Le comportement à la corrosion chimique des couches minces de ZNO par SPRY pyrolyse, Mémoire de Master, Mohamed Kheider Uuniversity-Biskra, 2013

**[28]** François Brisset, Jacky Ruste, Microscopie électronique à balayage - Principe et équipement, Réf : P865 v4, 2024

**[29]** https://www.techno-science.net/glossaire-definition/Microscopie-electronique-a-balayage-page-2.html

**[30]** https://mima2.jouy.hub.inrae.fr/equipements/microscopie-electronique/microscopie-electronique-a-balayage

**[31]** https://mea.edu.umontpellier.fr/meb/

**[32]** https://www.cea.fr/comprendre/Pages/nouvelles-technologies/microscopes.aspx?Type= Chapitre& numero=2

**[33]** Abdel Majid Aldimassi, Elaboration et caractérisation magnétiques et structurales de nanostructures de FeCoB optimisées pour des applications radiofréquences, Thèse de Doctorat, Bretagne occidentale University- Brest, 2020
**[34]** H. Ghorbani et al., Study on the effects of cadmium and chromium substitution in hydrothermally-synthesized spinel cobalt ferrite nanoparticles, Eur. Phys. J. Plus, 138:822, 2023

**[35]** Xiaoyan Huang et al., Study on the structure and magnetic transformation of magnesium substituted cobalt spinel-type ferrite, J Mater Sci: Mater Electron, 34:190, 2023

**[36]** Ehab A. Okba et al., Design of silver‑zinc‑nickel spinel‑ferrite mesoporous silica as a powerful and simply separable adsorbent for some textile dye removal, Scientific Reports, 14:16481, 2024

**[37]** Davood Gheidari et al., Synthesis and potent antimicrobial activity of CoFe2O4 nanoparticles under visible light, Heliyon, Vol. 6, e05058, 2020

**[38]** Asfeeaz Chaudhar, et al., Dye degradation and antimicrobial applications of manganese ferrite nanoparticles synthesized by plant extracts, Chemical Physics Impact, Vol. 5, 100098, 2022

**[39]** Devi A. Gole et al., In vitro antimicrobial activity of cobalt ferrite nanoparticles synthesized by co-precipitation method, Acta Chemica Iasi, 28_2, 225-236, 2020

**[40]** Reihaneh Haghniaz et al., Anti-bacterial and wound healingpromoting effects of zinc ferrite nanoparticles, Journal of Nanobiotechnology, 19:38, 2021

**[41]** Rauf Foroutan et al., Evaluation of two cationic dyes removal from aqueous environments using CNT/MgO/$CuFe_2O_4$ magnetic composite powder: A comparative study, Journal of Environmental Chemical Engineering, 2020

**[42]** A. Hakeem et al., Effect of multiwalled carbon nanotubes on Co-Mn ferrite prepared by co-precipitation technique, Digest Journal of Nanomaterials and Biostructures, Vol. 11, N°1, 149 – 157, 2016

**[43]** Ali A. Ati, Alyaa H. Abdalsalam, and Ali S. Hasan, Thermal, microstructural and magnetic properties of manganese substitution cobalt ferrite prepared via co-precipitation method, J Mater Sci: Mater Electron, 32:3019–3037, 2021